TOPICAL REVIEW • OPEN ACCESS

Effects of porosity on the mechanical properties of additively manufactured components: a critical review

To cite this article: Ahmad Y Al-Maharma *et al* 2020 *Mater. Res. Express* **7** 122001

Materials Research Express

TOPICAL REVIEW

Effects of porosity on the mechanical properties of additively manufactured components: a critical review

Ahmad Y Al-Maharma, Sandeep P Patil and Bernd Markert

Institute of General Mechanics, RWTH Aachen University, Eilfschornsteinstraße 18, 52062, Aachen, Germany

E-mail: patil@iam.rwth-aachen.de

Keywords: strength, stiffness, toughness, fatigue life, keyholes

OPEN ACCESS

RECEIVED
3 August 2020

REVISED
9 November 2020

ACCEPTED FOR PUBLICATION
19 November 2020

PUBLISHED
2 December 2020

Abstract

In the present review, the effect of porosity on the mechanical properties of the fabricated parts, which are additively manufactured by powder bed fusion and filament extrusion-based technologies, are discussed in detail. Usually, additive manufacturing (AM) processes based on these techniques produce the components with a significant amount of pores. The porosity in these parts typically takes two forms: pores with irregular shapes (called keyholes) and uniform (spherical) pores. These pores are present at different locations, such as surface, sub-surface, interior bulk material, between the deposited layers and at filler/matrix interface, which critically affect the corrosion resistance, fatigue strength, stiffness, mechanical strength, and fracture toughness properties, respectively. Therefore, it is essential to study and understand the influence of pores on the mechanical properties of AM fabricated parts. The technologies of AM can be employed in the manufacturing of components with the desired porous structure through the topology optimization process of scaffolds and lattices to improve their toughness under a specific load. The undesirable effect of pores can be eliminated by using defects-free raw materials, optimizing the processing parameters, and implementing suitable post-processing treatment. The current review grants a more comprehensive understanding of the effect of porous defects on mechanical performance and provides a mechanistic basis for reliable applications of additively manufactured components.

Abbreviations

μ-CT:	Micro-Computer Tomography.
ABS:	Acrylonitrile Butadiene Styrene.
ALS-LGCP:	Augmented Layer-wise Spatial Log Gaussian Cox Process.
AM:	Additive Manufacturing.
BAAM:	Big Area Additive Manufacturing.
CCF:	Continuous Carbon Fiber.
CF:	Carbon Fiber.
CFF:	Composite Filament Fabrication.
CNTs:	Carbon Nanotubes.
CT:	Computer Tomography.
DMLS:	Direct Metal Laser Sintering.
EBM:	Electron Beam Melting.
FEM:	Finite Element Method.
FFF:	Fused Filament Fabrication.
FGAM:	Functionally Graded Additive Manufacturing.

HDPE: High-Density Polyethylene.
HIP: Heat Isostatic Pressing.
IF-WS2: Inorganic Fullerene Tungsten Sulphide.
LB-PBF: Laser Beam- Powder Beam Fusion.
LSAM: Large-Scale Additive Manufacturing.
ME: Material Extrusion.
NFRC: Natural Fiber-Reinforced Thermoplastic Composite.
PBF: Powder Bed Fusion.
PC: Polycarbonate.
PDT: Probabilistic Damage Tolerance.
PEEK: Polyether Ether Ketone.
PMMA: Polymethyl methacrylate.
RVE: Representative Volume Element.
SEM: Scanning Electron Microscopy.
SLA: Stereolithography.
SLM: Selective Laser Melting.
SLS: Selective Laser Sintering.
SR-T: Synchrotron Radiation Microtomography.
Ti-6Al-4V: Titanium-6Aluminum-4Vanadium.
TPMS Triply- Periodic Minimal Surface.
TPU Thermoplastic Polyurethane.
UTS Ultimate Tensile Strength.
VED Volumetric Energy Density.

1. Introduction

The technologies of AM are highly appropriate for many critical applications in the aerospace and medical sectors [1]. The AM can be defined according to the American Society for Testing and Materials (ASTM) as 'the process of joining materials to make objects from three-dimensional (3D) model data, usually layer upon layer, as opposed to subtractive manufacturing methodologies'. From this definition, it can be inferred that there is no need to use special tools such as molds to form the shape of the manufactured parts since the manufacturing operation depends on the data (shape and dimensions) retrieved from the geometry model loaded to the printing machine [2, 3]. There are two frequently used methods implemented in various applications of AM: powder bed fusion and material extrusion-based three-dimensional printings.

Powder bed fusion is one of the most efficient AM techniques used in the fabrication of components of complex shapes using the thermal energy of the laser beam to fuse selected regions of a powder bed. Under this technique, three different processes can be found: SLM (termed as LB-PBF according to ASTM), SLS, and EBM. The SLM is nearly similar to SLS. Nevertheless, the primary distinction is using high power laser during the SLM process that melts the powder into a 3D solid part. One of the attractive advantages of the PBF method is the possibility to use a broad range of materials as feed-stock, including polymers, ceramics, metals, and composites [4]. For instance, the SLS machine can process many types of polymers, including polyamide and semi-crystalline thermoplastics (PEEK, PCL, and polyethylene) [5]. The quality of the parts produced by PBF processes is mainly affected by the state (virgin or recycled), shape, and size of the powder particles. The powder samples that have considerable loading of particles with irregular shapes, or small-sized ones could have significantly reduced or inconsistent flow rates or both of them [6]. The material powder should be free from undesirable quantities of impurities and inclusions. The recycled powder is allowed to be mixed with virgin powder at appropriate proportions determined by the raw materials' supplier. The recycled powder should be sieved with a sieve having a mesh size suitable for eliminating any contaminants or agglomerates from the manufacturing cycle [7].

Material extrusion is another AM technique that selectively dispenses the melted material through a nozzle to fabricate a three-dimensional part. There are three main printing processes classified under this technique: FDM, FFF, and Direct Ink Writing [4]. The FDM system is composed of the following main elements: raw material feed mechanism, liquefier, printing head (nozzle), gantry, and material deposition surface [5]. The

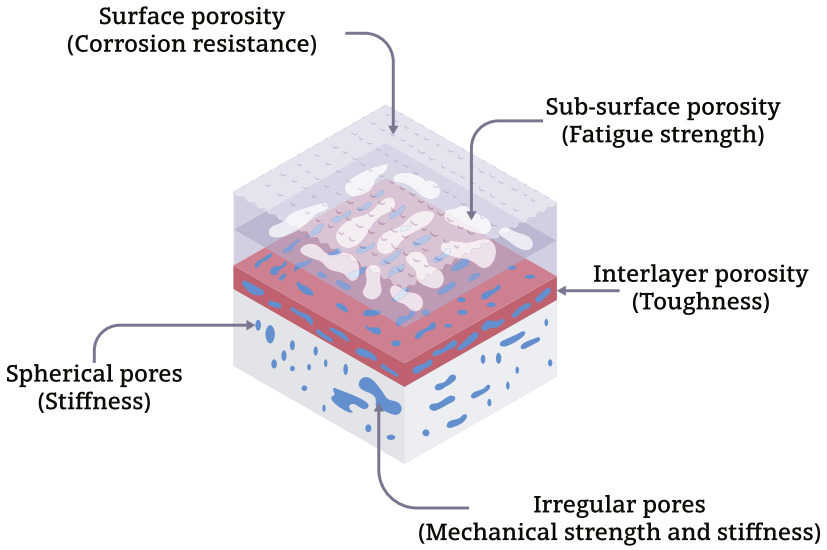

Figure 1. The effect of types and locations of pores on the mechanical properties of AM processed material.

traditional design of the FDM printer usually uses a single melted filament of material to build a three-dimensional object. The FDM printing machine used to process thermoplastic polymers, which is the most widely used printer across all printing machines found in the family of ME machines due to its less wastage of raw materials, ease of use, and low cost. The process of FFF is similar to that of FDM since they share the same printing principle in which the heated nozzle is used to melt the material filament before its deposition onto a moving platform. The FFF printing machines have advanced designs and capabilities such as dual filaments printing capability, which qualify them to fabricate parts composed of fiber composite and polymer blends [8, 9]. Generally, the FFF process builds parts that have significant flaws, such as high anisotropy, which describes the degree of variation in material properties when they are characterized in in-plane and transverse directions, weak mechanical strength, and high deviation in the dimensions relative to that of ideal geometry loaded to the printing machine. These downsides cannot be easily manipulated, which subsequently limit the practical implementations of the FFF process in critical applications found in the aerospace and biomedical industries. However, the FFF process contains several printing parameters that enable the user to reduce the undesirable effect of these drawbacks on the mechanical performance of the manufactured parts, including layer thickness, printing temperature, infill style, and infill percentage. For instance, the bond strength between the deposited beads can be effectively improved by adjusting the printing temperature and deposition rate to be compatible with the type of material implemented in the FFF process. It is noteworthy that there are a limited number of studies investigating the degree of adhesion strength between the layers processed by the FFF process. Therefore, further research is needed to improve the interlayer adhesion by either using adhesive materials or by suggesting novel *in situ* treatments to improve the adhesion strength among the printed beads [10].

In summary, the mechanical performance of the parts produced by the PBF and ME processes is still below the requirements needed for the structural applications since it is mainly affected by structural defects, such as porosity that unintentionally emerged during the production stage. Thus, it is essential to study the effect of these flaws on the physical and mechanical properties of the produced parts to suggest efficient solutions that can alleviate their harmful impact on structural integrity. However, this topic is not yet adequately understood, as well as a detailed review is also not present in the literature. Therefore, this work provides a well-organized literature review that offering a comprehensive perspective of both negative and positive aspects of porosity generated in the structure of AM fabricated parts. Moreover, this review discusses the latest methods developed to minimize the undesired impact of voids, such as: (i) controlling the distribution of pores in printed structure to increase the load-carrying capability of the three-dimensional printed part, (ii) developing modifications on existing AM machines or integrating them with conventional manufacturing methods, (iii) optimizing the processing parameters of the printer and linking them with pores' detection and quantification methods, and (iv) combining two or more post-processing treatments.

2. Porosity as defects and functional structures

In this section, the dual functions of porosity that could play in the structure of AM fabricated part as a structural flaw and engineered porosity are discussed in detail. According to ASTM definitions, the porosity in AM can be classified into two main kinds: (i) Apparent porosity corresponding to porous defects that are formed unintentionally in the well-prepared structure and/or at the unetched surface of the additively manufactured material [11]; (ii) Engineered porosity that is intentionally created and controlled for an engineered performance and a particular function. The porosity usually owns physical properties, including size, dimensions, shape, and architecture, which can be produced through a controlled fabrication process [12]. In recent years, additively manufactured materials have been extensively studied computationally and experimentally to understand the effect of porous defects on critical mechanical properties, such as stiffness, strength, and toughness. According to figure 1, pores can be detected at three critical locations of AM processed materials: at the excessive rough surface, sub-surface, among deposited layers, in addition to the internal bulk material [13].

The inter-layer pores are very decisive to the toughness properties of the part when the loads are applied transverse to the layer orientation since these defects induce the delamination among the deposited layers. The remaining locations, where the porous defects are distributed, critically affect tensile and fatigue strengths since they act as damage initiation sites under tensile and cyclic loading [9, 14, 15]. The rough surface decreases the corrosion resistance of the AM fabricated parts, especially those made from metals when exposed to high aggressive corroding medium [16, 17].

Recently, cellular materials find a wide area of applications in defense and biomedical industries. The porosity in lattice structures and scaffolds can be engineered to fulfill the requirements of mechanical properties and biodegradation behavior needed to replace the damaged organs in the human body. Furthermore, in the defense sector, the cellular materials can be used as structural support for the core of sandwich composites, which are designed to resist high amounts of dynamic loads. This implementation can be attributed to the capability of AM processes on customizing the design of single unit cell and the subsequent cellular structure to meet the required stiffness and toughness values in specific directions subjected to load application. It should be noted that in 3D printed cellular materials, the periodic boundary conditions (including types of applied loads), in addition to the type, size, and orientation of unit cells, typically influence the mechanical properties, porosity, damage mechanisms, and deformation of the resulting printed part [18].

The quantity and distribution of air pores in AM processed material are totally dependent on the AM process. Mainly, the porosity influences the mechanical performance of parts produced by PBF and filament extrusion-based AM processes, while those printed by SLA exhibit excellent strength and improved anisotropy due to the functional adhesive bond strength attained from the polymerization of the new layer with previous one. Consequently, porosity influences in a dramatic way the quality and reliability of the printed materials, and removing or at least minimizing these unfavorable effects is of the highest importance in real-life implementations [19, 20].

2.1. Porosity in materials processed via PBF

Three different types of pores are observed in the parts fabricated by PBF as follows: (i) functional pores, which are open and connected pores resulting from de-binding. These pores can be removed by using low melting point raw materials, heat and pressure post-treatment, and infiltration with compatible secondary materials to attain fully dense composite components. (ii) microstructural pores: residual defects and voids existed in the microstructure of the fabricated part; they are created unintentionally and should be minimized or avoided to alleviate their negative impact on mechanical properties and to guarantee the consistency of additively manufactured parts. (iii) structural (engineered) pores: intentional pores which are introduced for a particular purpose like pores in biomedical scaffolds that enhance nutrient delivery and tissue in-growth, or empty cells in lattice structures, which decrease the overall weight without any effect on the loading capacity of the component [21]. The microstructural pores can take two primary forms in the structure of PBF processed materials: (i) spherical pores resulting from a powder containing entrapped gas introduced by gas atomization process of powder particles, (ii) keyholes, which are formed when the processing parameters are incorrectly set. For example, when the nozzle temperature or energy density is insufficient to melt the powder, the pores with irregular shapes can be detected in the structure of the produced part [22, 23]. The formation of the pore, especially spherical shaped one, is considerably affected by the characteristics of raw materials. These characteristics include distribution, size, shape, the ease of flow through printing, composition, and surface morphology of the powders. The powders with uniform size distribution promote good mechanical properties, structure morphology, homogeneous melting, interlayer bonding strength, and surface finish [24, 25].

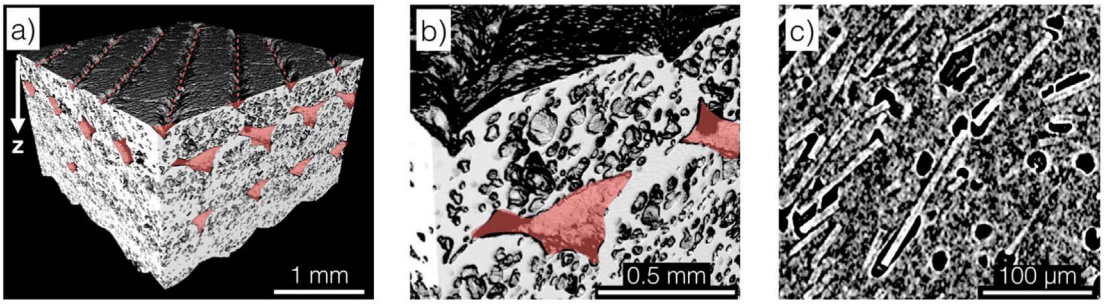

Figure 2. Pictures retrieved from x-ray CT for CF/ABS composite with 100% infill showing: (a) inter-bead porosity highlighted in red, (b) beads with intra- and inter-bead porosity, (c) pores at the fiber-matrix interface [27].

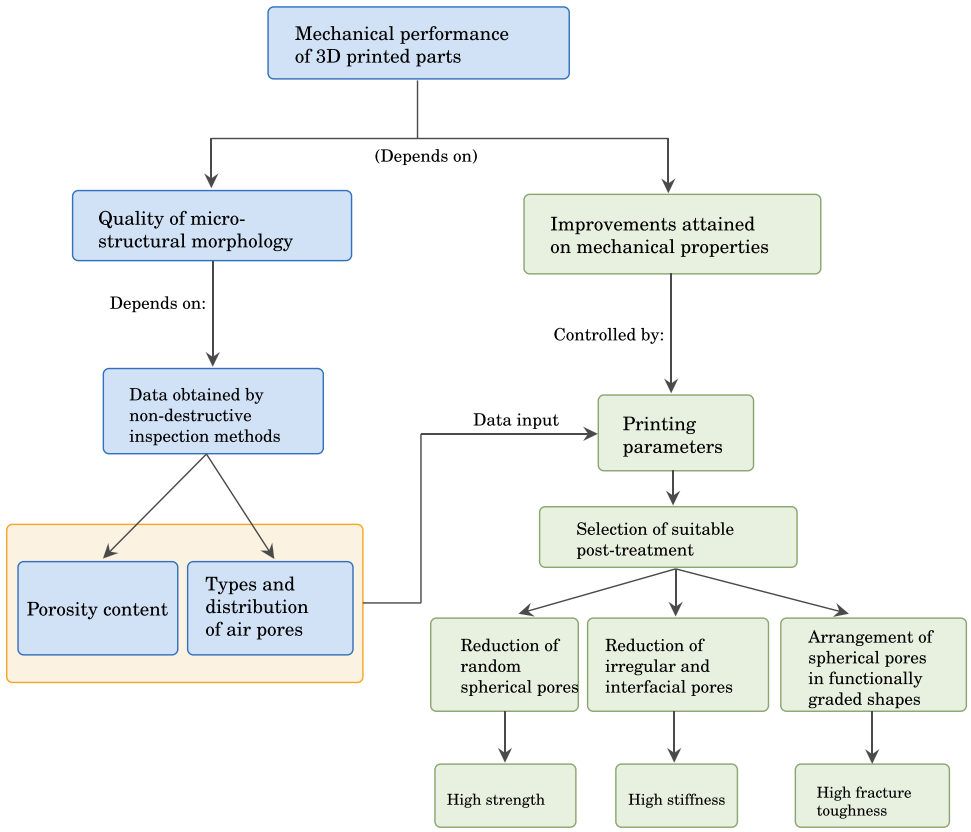

Figure 3. The relationship between microstructure and property and the role of porosity detection methods.

2.2. Porosity in materials printed through ME

Two main types of voids can be identified in FFF processed fiber polymer composite, as demonstrated in figure 2: intra-bead and inter-bead voids. The intra-bead pores are the most critical, which can be reduced by improving fiber-matrix adhesion and choosing high-quality printing filaments. The nozzle geometry of the FFF printer causes the inter-bead pores, and by enhancing the shape of the nozzle exit, this can be managed down to a minimum [26, 27].

In the parts fabricated by ME processes, pores form linear patterns at the interfacial region between deposited beads due to the layer-by-layer based printing strategy. The extrusion of the melted substance onto the solidified one from formerly deposited layers could be the leading cause for pores generation, which therefore leads to stress concentration and premature failure in 3D printed components due to weak bond strength between adjacent beads [28]. The porosity and the variation in orientation between deposited beads create remarkable anisotropy in the material properties of the parts fabricated by ME based process. One familiar technique to reduce the anisotropies in the properties of printed objects is modifying their orientation through the manufacturing process. Other possible measures include finishing processes after every layer printing, such as mechanical or chemical polishing, or post machining after the building operation is completed [18].

The fiber composites characterized by high mechanical performance can be produced through ME processes if the requirements of minimal porosity and fiber alignment are fulfilled. The values of mechanical strength and elastic modulus of ME produced composites are lower compared to their counterparts processed through traditional manufacturing processes such as compression and resin transfer moldings. The main reason behind this is justified to the agglomeration of fibers in highly viscous filament melt along with high internal porosity that emerged from the weak adhesion strength at the fiber /matrix interface in addition to the partially independent movement of matrix and fibers through the extrusion process [29]. For example, CNTs are used to increase the strength of PEEK polymer. However, the tensile strength is decreased with higher contents of these fillers due to the formation of more pores in the highly viscous melt. It should be noted that the single feed-sock-extrusion nozzle design of commercial filament extrusion-based printers is incapable of resolving this issue while redesigning the raw materials feeding system to accept separate feedstock of material and reinforcing filler is considered a reliable approach for 3D printing of composite materials. Moreover, the anisotropy rise in the mechanical properties of fiber composites can be further reduced by changing the direction of nano-fillers to make them orienting with the filament. These fillers tend to align themselves in the direction of extrusion [30].

3. Detection and quantification of porous defects

In recent years, different methods have been developed to explore and quantify the porosity formed in the structure of additively manufactured parts and their subsequent effect on their morphological and mechanical properties. In order to improve the quality of printed parts, two basic requirements are needed: (i) development of appropriate techniques to detect the microstructural defects and pores generated in location; (ii) reduction of residual porosity [21]. A good comprehension of the material anomalies and main failure modes is essential and should be connected to fabrication process parameters and non-destructive inspection (NDI) methods. For a better fundamental understanding of the process-structure-property relationship described in figure 3, detailed theoretical investigations and multi-physics simulations, including thermodynamics, thermo-mechanical, fluid dynamics, and microstructural modeling, are needed. These models would aid in realizing the characteristics of the melt pool, densification, residual stress, and distortion, along with the behavior of customized material properties. Hence, there is a need to develop predictive models that can offer information describing the relationship between the final mechanical properties of strength, stiffness, toughness, and fatigue strength of the printed part and processing parameters of the AM method. A Gaussian process based predictive model accurately shapes the relationship between the porosity in AM fabricated part and processing parameters of the SLM process, which are mainly scanning speed and laser power. In this model, the best linear unbiased prediction is used to predict porosity at any required speed-power combination. Some statistical damage prediction methods are developed like PDT framework, which is commonly employed to assess the failure probability of aviation components in the existence of randomly distributed material defects and a combination of other deterministic and random factors. One significant benefit of the zone-based PDT evaluation is that it can measure the relationship between the design criteria (i.e., acceptable risk level) and some of the fabricating parameters or the critical material property, hence offering a desired feedback loop. Furthermore, the PDT framework can be used to assess post-treatment effect on reducing the levels of tensile residual stresses and surface roughness, respectively [23, 31, 32].

The accuracy of the analytical and numerical results obtained through porosity prediction models can be enhanced if they are linked with experimental porosity measuring techniques such as x-ray CT. For example, a high-speed digital camera is used for in-process sensing of melt pool data by inserting it co-axially close to the laser beam in the laser-based AM process. The porosity properties inside the deposited samples are retrieved using cross-sectioning and x-ray CT. The features of melt-pool, including porosity attributes, are analyzed through a convolutional neural network (CNN) derived predictive porosity models with detection and classification accuracy of 91.2%. For pores to be captured by the camera, they should produce an adequate effect on the melt-pool behavior with pore size higher than 30 μm [33]. The ALS-LGCP approach quantifies the distribution of spatial pores within every layer of the 3D printed part and follows their sequential evolution across layers. The ALS-LGCP model represents the pores appeared at x-ray CT images of AM fabricated part through patterns of augmented point, including information about the size, number, and location of the pores. Furthermore, it implements the spatial correlations between pores for recognizing areas susceptible to pores on various deposited layers [34].

There are many methods available for measuring porosity experimentally [35]. One of these techniques is the Archimedes method, which is the basic non-destructive technique for measuring the porosity of the whole specimen. The volume fraction of pores is approximated from the density of the printed part evaluated using this technique. Nevertheless, the data about size, shape, and distribution of pores cannot be extracted using this method. According to Archimedes (weighing) method, the average porosity is calculated from the following

relation:

$$Porosity\,(\%) = \left(1 - \frac{\frac{W_s}{V_s}}{\rho_t}\right) \times 100 \tag{1}$$

where: W_s and V_s are the weight and bulk volume of the porous sample, ρ_t is the theoretical density of pure material [36].

The adsorption process between gas and solid at equilibrium is usually investigated through adsorption isotherm models indicating the adsorbate's quantity on the adsorbent as a function of its concentration or partial pressure at a constant temperature. Usually, the adsorbed amount is normalized by the total adsorbent's mass to compare various materials [37, 38]. The multi-molecular adsorption model proposed by Brunauer, Emmett, and Teller (BET) is one of the most widely used adsorption isotherm models for describing the gas adsorption onto a porous solid surface, which can provide a complete understanding of pores' size and their distribution in the structure. The specific surface area (SSA) and total pore volume are used as primary indicators to determine porous solid's adsorption capacity [39–41]. The surface area refers to a solid part's exterior surface area, including surface attributable to pores. The SSA (m^2/g) is defined as the porous structure's surface area divided by its mass. The volume-specific surface area (VSSA) (m^2cm^{-3}) is derived from the definition mentioned earlier by multiplying the SSA with the material density that does not include porosity. The nitrogen gas is commonly used in the BET method to measure the whole (gas accessible) exterior and interior surface areas of a given specimen. The values of SSA give clear indications about gas accessible external and internal surfaces, while these of VSSA are used to evaluate the porosity degree in the specimen [42, 43].

The vapors and gases that could be chemically or physically adsorbed onto the surface after manufacturing the sample and during its storage and handling should be eliminated to measure the porous solid's SSA using the BET volumetric method accurately. In this method and after degassing, the nitrogen gas (at 77 K) is used as adsorbate, which flows through the specimen's accessible regions to provide a specific equilibrium pressure. The amount of vapor adsorbed on the sample is evaluated by altering the pressure after equilibrium. The quantification of adsorbed vapor is repeated at various pressures to attain an adsorption isotherm through which pore volume, pore size distribution, and surface area can be specified [44]. The accuracy of porosity measurements is improved when the moisture free nitrogen gas is used to flow through an adequate sample quantity since the error is increased with smaller surface areas of the specimen [45]. According to the BET model, the following relation can be used to calculate the surface area of porous solid, assuming that the number of adsorption layer is infinite:

$$\frac{V}{V_{mon}} = \frac{c(p/p^0)}{1 - (p/p^0)[1 - (1 - c)(p/p^0)]} \tag{2}$$

where V is the total volume of adsorption, V_{mon} is the monolayer's volume, p is partial equilibrium pressure, p^0 is the saturation vapor pressure, c is a dimensionless constant related to the heat of adsorption, which can be evaluated from:

$$c = \exp\left(\frac{\Delta H_1^0 - \Delta H_2^0}{RT}\right) \tag{3}$$

R is gas constant ($J\,K^{-1}\,mol^{-1}$), T is the temperature (K), ΔH_1^0, and ΔH_2^0 are the standard adsorption enthalpies for the first and subsequent layers ($kJ\,mol^{-1}$), respectively. The value of V_{mon} can be retrieved from the linearized form of equation (2) as follows:

$$\frac{p}{V(p^0 - p)} = \frac{1}{V_{mon}c} + \frac{c - 1}{V_{mon}c}\frac{p}{p^0} \tag{4}$$

At higher values of c, the intermolecular interaction is lower than that between vapor molecules and surface. The multilayer adsorption process begins with increasing pressures [44, 46]. There is a limitation in the BET model related to porosity characterization at supercritical conditions since the p^0 in equation (2) is not defined if the temperature is higher than the adsorbate's critical temperature. Therefore, at these special conditions, the pressure is replaced with density [47].

Optical microscopy is a widely implemented destructive technique to measure porosity. However, the volume fraction of the pores cannot be accurately determined through this method. Furthermore, this technique is not appropriate for measuring quite small pores with a size smaller than 50 μm. On the other hand, SEM, SR-T, and x-ray CT scans accurately measure the distribution, size, and shape of tiny pores. The CT scan effectively measures pores as small as 10 μm, while the SR-T technique can be implemented to measure the *in situ* formation of porosity [24]. The CT offers a detailed 3D information regarding the size, shape, and distribution of pores, how porosity differs in and across the build direction, and how pore structure differs

among parts with similar levels of porosity but processed at different processing parameters [48, 49]. With the support of x-ray CT, the geometric deviations from the standard design can be accurately detected and pictured [50, 51]. It is noteworthy that this porosity measuring technique may give a faulty indication about more substantial porosity content higher than controlling reference values. This deviation is originated from lower sharpness of CT data, averaging, and reduction of information quantity upon magnification reduction [52]. Therefore, a piece of prior knowledge about the critical size of defects should be established to select suitable experimental setup to detect such significant flaws, including porosity. Small defects detecting equipment with high-resolution capability are unable to manipulate the large volume of data, thus set the need for choosing RVE to test in the laboratory [21]. The x-ray CT scan provides a useful qualitative visualization of pores, while the quantitative outcomes depend on the accuracy of the threshold selection of x-ray CT images [48]. The metallographic image, which shows the material pores with higher contrast relative to other components, can be implemented as a reference image for the threshold selection of CT samples [53].

Neutron tomography/radiography provides distinct imaging capabilities over a broad range of applications, including fiber thermoplastic composites. The neutron imaging technology offers reliable information about the location and size of pores in the laminated printed structure. This feature will enable the composite material designers to choose the suitable processing parameters in order to achieve a flawless automated fiber placement part fabrication. At the preliminary stage, the porosity in the fiber composite laminates can be investigated through a conventional optical microscopy method. The main benefits of this method are its acceptable accuracy, simplicity, and no need to use hazardous or costly materials [54]. A quantitative measure for the internal porosity of FFF-fabricated objects is developed based on the ultrasonic imaging system with spatial resolution in the range of 1.0 and 200 μm. The measuring system is composed of highly damped ultrasonic probes, which are used to gather data in pulse-echo and through-transmission modes, and coupled with a three-axis scanner. The collected data through ultrasonic probes are processed to create peak to peak amplitude C-scan images. These images are used to visualize the conditions of inner and outer surfaces, the presence of internal flaws, and the regions of unexpected process flaws [55].

The μ -CT scan can be used to quantify the internal and sub-surface pores in micro-sized 3D printed components and the determination of pores' types in 3D printed structure [56]. With the aid of the μ-CT scan, the average area porosity can be determined as the percentage of the ratio between the area of pores to the cross-sectional area of the sample [57]. Additionally, the μ-CT measuring technology is used in benchmarking the performance of 3D printers by coupling it with advanced manufacturing software packages. Having better feedback on printing fidelity motivates the standardization of 3D printed material performance and facilitates the assessment of 3D bioprinting [58]. Moreover, a μ-CT scan can be used to effectively capture the interfacial pores between the neighboring layers of AM processed materials, including lattice structures [59]. Through controlling the quality of 3D printing at the interfacial region between layers, the inter-layer tensile bond strength can be adequately enhanced [60].

The properties of additively manufactured microstructure are usually studied through Xray diffraction, transmission electron microscopy, and optical microscopy [61]. New optical microscopy scanning methods are developed recently, one of these methods called Morphologi G3 technique, which is used to quantify the pore size distribution and micro-cracks in AM processed metallic parts with high detection precision (around 1.75 μm) [62, 63]. For instance, the optical emission microscopy is employed for in-process monitoring of porosity in part made of nickel alloy 718 processed by LB-PBF. After the printing process, the content of porosity is quantified through x-ray CT. This approach provides reliable porosity prediction on the layer-by-layer scheme with an accuracy of 90% and computation time less than 0.5 seconds [64].

The predictive equations describing the relationship between pore arrangement, pore geometry, and orientation with mechanical properties over a wide range of porosity are not developed yet [65, 66]. Therefore, FEM is considered as a useful prediction tool to study the effect of the porosity properties mentioned earlier on the mechanical properties of AM fabricated part. The accuracy of FEM prediction of porosity impact on mechanical properties such as fatigue strength of AM processed parts can be significantly improved through using data generated from fracture surface analysis and x-ray CT as inputs for FE-model [67]. FEM based modeling can be used to represent 3D printed composites reinforced with short and continuous fiber. This type of modeling differs from usual models in terms of the significant content of voids that should be included in the model's geometry [5]. In any finite element analysis of 3D printed material, the shape, size, number, and orientation of pores should be defined in the RVE model [65]. It is important to note that it is impossible to design RVE with a porosity content of 28 vol.% without overlapping of pores. In addition, the pores' content should be proportional to that of reinforcing fillers since the increasing loading of reinforcements increases the content of porosity due to weak interfacial bonding with hosting polymer [68]. Besides structural analysis that evaluates the stiffness, strength, and fatigue properties of the AM fabricated parts, the computational fluid dynamic simulation can be used to generate detailed information about surface roughness, porosity, and bond line densities of inter and intra-layers of 3D printed components. The quantitative predictions of the aspects

mentioned above of the printed part emphasize the possibility of conducting numerical optimizations of the printing process parameters [69].

4. The effect of porosity on strength, stiffness, and toughness

The values of strength and stiffness for fiber composite materials processed by ME based processes are highly affected by the printing parameters (i.e., infill percentage and pattern along with printing speed and temperature), which create a remarkable difference between the reference values of strength and stiffness specified in the material catalog, and those characterized through experimental testing in the laboratory. Moreover, the high pressure and temperature conditions used in conventional manufacturing methods like injection molding significantly reduce the void content generated during part fabrication leading to high strength and stiffness values for parts produced through these techniques [70]. Short and continuous fibers, along with particles, are used to increase the strength and stiffness of printing filaments used in FFF/FDM machines. The excellent reinforcing fibers like carbon are used to increase the stiffness and strength of neat thermoplastic polymers processed by the FFF process to make their mechanical properties comparable to those of unidirectional epoxy matrix composites. Generally, there are two main approaches used in the processing of composite materials through the FFF technique: (i) The printing of short fibers with an average length of 0.1mm through conventional ME processes; (ii) The processing of continuous fiber through implementing a particular design of printing head. The incorporation of short fibers in printing filament increases the stiffness of the fabricated part. However, the improvement attained on strength is still limited since the fiber pull-out could take place before fiber breakage. Due to low porosity content, the short fiber printing fabricates parts with higher quality than those produced through continuous fiber printing. The mechanical strength of components built by short fiber printing can be further improved by reinforcing the thermoplastic filament with short fibers having an average length above the critical fiber length [29].

The stiffness and tensile strength of ABS filament are increased when it is reinforced with 10 vol.% of chopped carbon fiber. The multi-laminate structure processed by the FDM printer shows 29% higher in single shear and bearing strengths up to 63% higher in double than the equivalent machined/drilled sample representing the current industry standard for fastening performance [71]. In order to achieve the expected improvements on properties of printed composites, the fillers should be uniformly homogenized in the printing material and have a robust interfacial bond strength with it, which can be achieved normally using chemical functionalization. For example, composite filaments composed of hollow fly ash cenospheres homogeneously blended with 40 wt. % of HDPE can be used instead of pure HDPE filament to increase the strength and stiffness of HDPE parts processed by FFF-printer under optimized processing parameters [72]. Additionally, FFF-processed PC reinforced with CCF bundles composite shows an increase of 77% in tensile yield strength. The adhesion between PC and CF fabrics is confirmed to be strong according to the outcomes of the pull-out test [73].

The strength and elongation of the FDM fabricated part are increased significantly after incorporating 6 wt. % and 10 wt. % of iron (Fe) reinforcing powder in the filaments synthesized from recycled powders of HDPE and low-density polyethylene, respectively [74]. However, the increasing content of reinforcing fillers promotes the formation of pores in the filler-reinforced polymer printed structure due to the reduced filler/matrix contact area leading to poor load transfer from matrix to adjacent fillers. The mechanical strength of composite parts processed by AM increases with increasing load of fillers up to a specific limit due to large porosity generated at higher volume fraction (vol.%) of reinforcements. For instance, FDM processed CCF/nylon composite exhibits the highest increase in mechanical strength per fiber content with around 6.3 folds higher than the value of pure nylon polymer. With the continuous increase in CCF content, a moderate improvement in mechanical strength can be attained due to poor adhesion at CCF/nylon interface as well as the increased content of air voids [75].

The amount of increase in the porosity content of AM processed composites is directly proportional to the size of the reinforcement. Furthermore, the increasing content of inclusions in printing materials contributes to improving the dimensional stability of produced parts through minimizing shrinkage and distortion even they induce the formation of porosity. This conclusion can be deduced from the experimental printing of CNTs and short CF fillers used to reinforce the filament of ABS. It is noted that the shrinkage and deformation of composite samples are reduced upon the implementation of carbonous reinforcements in printing filament. The size of the pore increases in the order of ABS, CNTs/ABS, and CF/ABS samples. Because of porosity and various orientation of layers within the same structure of the printed part, the FFF/FDM processed fiber composite exhibits a strong anisotropy in terms of impact and flexural properties. This anisotropy can be reduced through fabricating the fiber composite material into one layer instead of conventional multilayer 3D printing. For example, a 0/90 woven structure is printed using FDM into one layer to improve stress distribution. The intra-layer air voids are reduced through the build-up of fibers, which exerts additional downward pressure on the

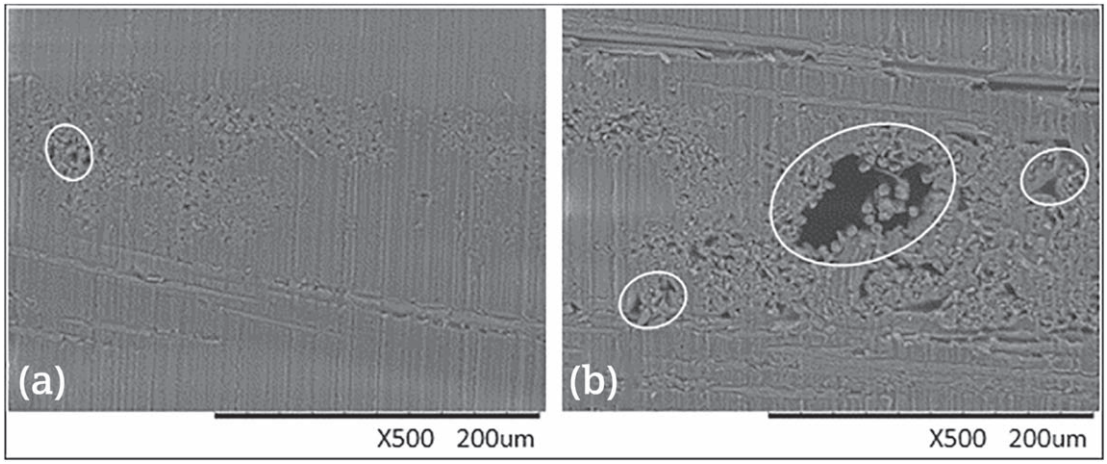

Figure 4. SEM images show air voids in (a) bulk structure and (b) near defected areas proving mitigation in porosity due to the increase in filament density. Reprinted from [76], copyright (2018), with permission from Elsevier.

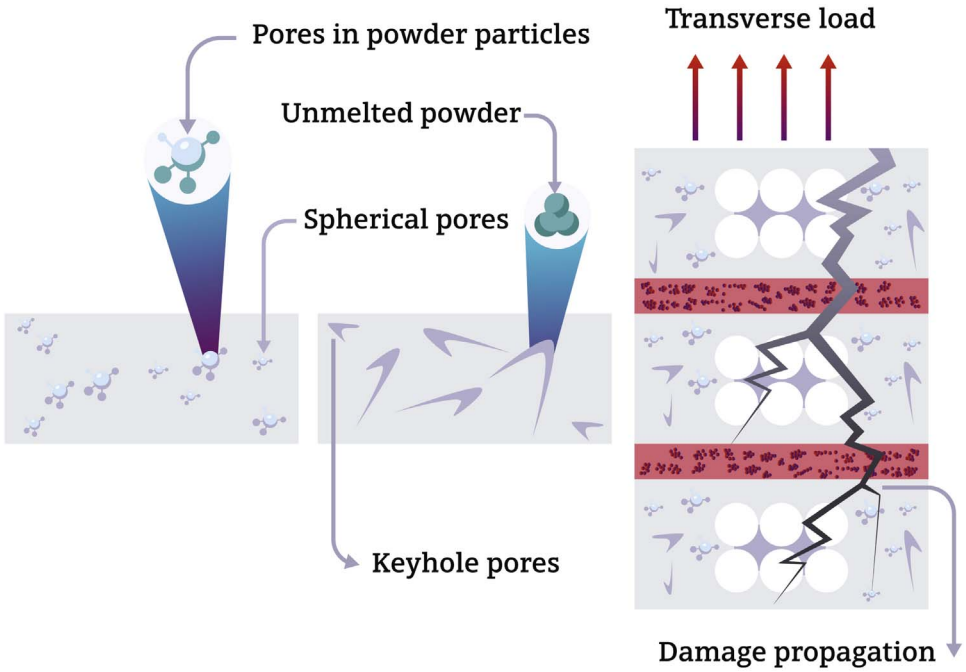

Figure 5. The effect of gas (spherical) and keyhole pores on the mechanical strength of fiber composite processed by PBF technology.

heated filaments and pushes air out of the structure, as demonstrated in figure 4, hence increasing stress distribution across the woven structure and load transfer efficiency in the porous regions [76, 77]. Other methods developed for reducing the anisotropy of composite materials are the implementation of functionalization and compatibilizers such as maleic anhydride to improve the adhesion and dispersion of fillers in the extruded polymer [78]. For instance, the phase aggregation and separation of graphene in 3D printed structure can be minimized through using oxidized functional groups of graphene oxide [79].

The surface, sub-surface, and internal porosity have a significant impact on the strength and stiffness properties of the parts produced by the processes of PBF. The surface porosity can be reduced in these parts by using finer powder particles, which leads to higher ratios of material transportation. The mixtures of two types of particles are more advantageous in mitigating porosity than mixtures composed of particles with arbitrary sizes [80]. It should be noted that the mechanical performance of materials processed by PBF technology is highly dependent on the state of used powder, whether it is new in the as-received state or recycled. Despite the fact that the microstructure of recycled and as-received powder deposits is similar, the contaminated particles considerably decrease the ductility through acting as brittle damage initiators (brittle inclusions) [81].

Table 1. The effect of porosity on mechanical properties of AM processed materials.

Material	Manufacturing method	Porosity (%)	YS (MPa)	US (MPa)	E (GPa)	ε%	References
Zr-2.5Nb alloy substrate	Rolling	—	634	660	87.3	13.8	[81]
Zirconium (recycled powder)	SLM	0.099 (Area %)	611	731	93	2.7	
Zirconium (as-received powder)		0.01 (Area %)	569	696	67.4	16.3	
Ti-6Al-4V	ASTM (F2924-14)	—	825	895	—	10	[7]
	Wrought	—	806.7	851.4	119.3	13.5	[83]
	SLM	45.5%	146.6	194.9	10.4	7.8	
	SLM (cubic lattice)	63%	113	185	4.84	11.83	[84]
	SLM (diamond lattice)	40%	181	209.68	20.3	2.49	[85]
	SLM (cellular)	68.46%			18.4	—	[86]
Ti-6Al-4V/PEEK	SLM (cellular) coupled with polymer injection	—	—	—	26.46		
Titanium	Annealing	—	925	1015	115	5.2	[87]
	SLM+HIP	67.76%	55.13	144.32	2.14	59.8	[82]
Pure iron	Annealing	—	55.16	206.84	206.84	27	[88, 89]
	SLM (functionally graded)	58.4%	53.56	397.29	2.86	62.2	[36]
Stainless steel 316L	ASTM (F3184-16)	—	205	515	—	30	[90]
	Annealing	—	220	520	193	40	[91, 92]
	SLM (TMPS-like structure)	72%	66.48	223.47	9.23	40.4	[93]
	SLS	2%	—	518	—	61.9	[94]
Nickel super alloy (718)	ASTM (F3055-14a)	—	600	920	—	27	[95]
	Isothermal forging	—	1034	1276	199.95	12	[96]
	DMLS	5%	926.25	1128	228.1	17	[97]
TPU	bulk material	—	43.6	64.9	0.012	367	[98]
	SLS (auxetic lattice)	Full melting	—	14.25	—	511	[99]
Nylon 12	Bulk material	—	33.54	42.61	1.40	339.51	[100, 101]
	SLS	—	32.5	38.7	1.35	16.4	[102]
ABS	Bulk material	—	42.65	40.12	2.53	6.81	[103, 104]
	FDM (Kagome truss)	97.44%	0.43	0.58	0.019	3.48	[105]
Al/PLA	FDM	Unpolished	—	41.10	0.78	60.77	[106]
	FDM+Laser polishing	Polished surface	—	54.85	1.078	31.62	
CCF/PLA	Hot compression molding	—	—	1047	72.2	—	[107]
	FFF	7.5 vol.%	—	905.3	69.4	1.27	

The gas and keyhole pores are the primary porous defects responsible for the reduction that occurred on the mechanical strength of parts fabricated by PBF based processes. The keyholes act as stress concentration points inside the printed structure, where cracks can be easily initiated from them to the neighboring healthy regions. The porosity can play a very decisive role when the fiber composite materials are fabricated through PBF based processes since the porous flaws are distributed at critical locations, as demonstrated in figure 5. When a transverse tensile load is applied on the fiber composite, the interlaminar cracks promote the separation of printed layers in a short time duration due to a high amount of interlayer porosity. Therefore, there is a need to use external equipment that should be part of the PBF printing machine to apply an adequate amount of pressure that is sufficient to remove at least the interlayer pores beside the heat retrieved from the laser beam [30].

Typically, the increasing values of average porosity in SLM processed materials reduce their yield strength (YS), ultimate strength (US), and Young's modulus (E) properties under both tension and compression loading conditions as it can be anticipated from the values listed in table 1. By comparing the mechanical properties of SLM processed materials, it can be noted that the porous defects formed in the strut of cellular materials have a higher undesirable impact on mechanical performance compared with bulk and fiber composite materials. However, the strain to failure values (ε%) indicates that air pores, especially the functionally graded ones, increase the ductility of 3D printed materials due to the effective shear deformation mechanism taking place in the fabricated structure [36, 82].

The mechanical properties of cellular materials fabricated by the PBF process can be improved by filling their porous structure with secondary material characterized with enhanced mechanical performance such as PEEK polymer used to fill the cellular structure of titanium alloy (Ti-6Al-4V) [86]. The surface treatment methods

improve the US and E of materials processed by ME processes such as FFF and FDM even if the printed structure contains high contents of porosity. For example, laser polishing is used to improve the US of aluminum reinforced polylactic acid (Al/PLA) composite processed by the FDM printer at the expense of ε % property [106].

5. The influence of porosity on fatigue properties

The excessive surface roughness and sub-surface porosity of additively manufactured components have a noticeable contribution to the initiation of fatigue damage since these defects act as stress concentration locations [108–110]. The subsurface porosity or open surface pores make the part exposed to premature failure under the effect of cyclic loading. Thus, it reduces the fatigue strength of the parts fabricated by AM processes [111, 112]. Because of these porous defects, the fatigue resistance performance of the parts manufactured by ME and PBF technologies is lower than that of the parts fabricated by conventional manufacturing methods. For example, the number of cycles to failure of FFF-processed ABS is 60,000 cycles (at maximum stress $<$10MPa), which is quite low relative to 6.0 million cycles recorded to the same material fabricated through injection molding [113].

Moreover, the metallic parts manufactured and formed through conventional manufacturing processes such as rolling have high fatigue and corrosion fatigue properties compared to those formed through the SLM process. For instance, the wrought maraging steel 18Ni-C300 has higher fatigue performance than SLM processed counterpart due to its lower surface roughness in addition to its homogeneous and dense microstructure [114].

The cyclic plasticity effect leads to a local mean stress relaxation, which has a direct correlation with pore geometry. For internal gas spherical pores, the fatigue performance has a higher sensitivity to the location and shape of pores than the size. For instance, the fatigue strength of SLM processed Ti-6Al-4V is affected to the greatest extent with the shape and location of internal pore over other parameters such as pore size [115]. In the fatigue resistance point of view, the uniformly distributed and spherical shape porosity is not harmful to the structural integrity relative to large-sized keyholes. The keyhole defects with average length higher than 1mm considerably mitigate ductility, ultimate tensile strength, as well as facilitate the initiation of fatigue crack and decrease the fatigue life [116]. Additionally, the lack of fusion pores located at the surface of SLM processed Ti-6Al-4V alloy decrease the fatigue strength by 30% relative to its counterpart with a machined surface [117].

The enhancement in fatigue strength can be achieved through an additional reduction of surface roughness and internal porosity by the mean of heat and pressure treatments along with changing the printing parameters and scan strategy [118, 119]. The change in the microstructure of SLM processed Ti-6Al-4V alloy after the HIP post-treatment process at 150MPa/1000 °C alleviates the strain/stress concentration effects and enhances the fatigue performance under compression of the fabricated part [120]. Moreover, the fatigue strength of LB-PBF processed Ti-6Al-4V is significantly improved after the application of surface post-treatment. Therefore, after post-treatment, the fatigue strength value is influenced by the combination of microstructure, residual surface stress, surface roughness, and existing defects [121].

For constant levels of stress exerted on AM fabricated part, the high porosity contents lead to shorter fatigue life. For example, The fatigue behavior of LB-PBF processed Ti-6Al-4V is changed considerably at a volume fraction of porosity high than 5% [122]. Additionally, the fatigue strength of LB-PBF processed Inconel 625 alloy is found to be 590MPa at a porosity level of $\leqslant$0.1%. At the same time, this value is reduced with increasing porosity levels to be 280, 190, and 160 MPa at porosity contents of 0.3, 0.9, and 2.7%, respectively. This behavior is justified to the role of porosity in transforming the LB-PBF processed Inconel 625 from ductile to brittle material. It should be noted that the fatigue behavior of LB-PBF manufactured components cannot be correlated only to the porosity content, but rather, to the spatial position of pore whether at the surface or in bulk, geometry (lack of fusion pore or spherical pore) and size of individual (critical) pores [123].

The build direction of the parts fabricated by PBF processes has a significant impact on fatigue properties. For instance, samples of AISI 316L stainless steel are fabricated through SLM in vertical and horizontal building direction, leading to layer planes aligned perpendicular and parallel to the loading direction, respectively. The vertically built specimens show a lower fatigue lifetime relative to horizontally fabricated ones due to the higher surface roughness of the samples printed in the vertical direction [124]. Moreover, the fatigue strength of H13 steel processed by SLM is considerably affected by the pore's size, shape, and orientation relative to the build direction [125]. For instance, in the surface machined samples of stainless steel processed by LB-PBF, the fatigue cracks are initiated from subsurface pores having the size in the range of 20–30 μm [126]. Another important geometrical aspect is the part dimensions, which can effectively dominate the fatigue strength of LB-PBF processed Ti-6Al-4V alloy through changing one of the part dimensions such as thickness to affect the area of the

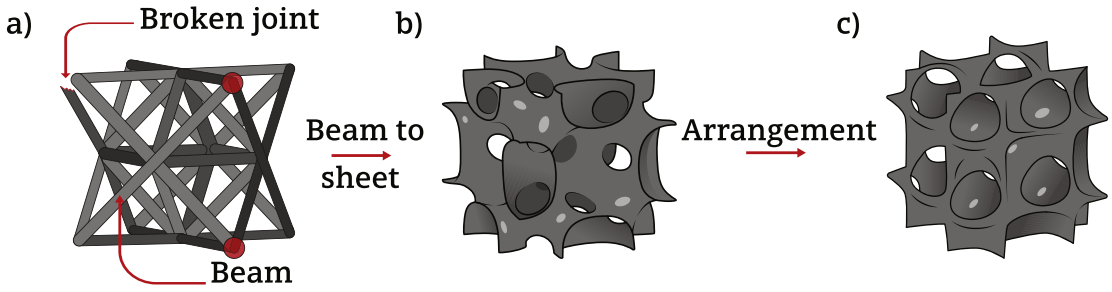

Figure 6. The smoothening of (a) thin wall-walled octet truss unit cell through replacing beams with sheets to produce shell lattices of (b) TPMS-like, and (c) diamond unit cells.

surface. The surface roughness, which introduces several micro-sized notches along the surface, has a considerable contribution to the mitigated fatigue strength of LB-PBF fabricated Ti-6Al-4V samples [127].

6. Improving toughness through engineered porosity

In this section, the role of PBF and ME printing technologies in improving the load absorption capacity of cellular and foam materials is discussed in detail. The aforementioned AM technologies, especially PBF, have an excellent capability of fabricating complex cellular materials, specifically those made from metallic powders. The structural designs, materials, and printing machines that can be used to increase the toughness of AM processed materials are discussed through the subsequent sections.

6.1. Enhanced toughness through lattice and scaffold structures

When voids are ordered periodically during the AM process, a material with engineered cellular structure like lattice or scaffold can be attained. The complex 3D geometries of scaffolds are characterized by a fully interconnected structure with pre-specified porosity and dimensions, which are needed for effective regeneration or repair of organs and tissues. A critical design property for tissue-engineered scaffolds is to enable an appropriate biological function in addition to mass transport (permeability and diffusion) along with mechanical integrity [86, 128]. The technologies of AM play a vital role in the topology optimization process of porous structures such as lattices and scaffolds to achieve a required functionality since the locations of material deposition in a defined domain can be accurately specified by AM machines based on numerical inputs of topology optimization analysis. The cellular materials provide to the part unique functional properties, including heat transfer control and heat dissipation, improved mechanical energy absorption capability, and high stiffness to weight ratio [18, 129]. The geometric freedom of AM can be employed in building internal structures that emulate a range of various material properties like Poisson's ratio, stiffness, toughness, and elastic limit depending only on a single build material. For example, the volumetric energy absorption capability of the diamond lattice structure is comparable to a wide range of standard aluminum foams. The voids in a lattice structure, such as diamond lattice, can be combined with other lattice structures with different designs. They may be filled with materials to offer secondary control of embedding functions such as sensing and energy storage [102].

The processes of AM can be combined with conventional manufacturing technologies to improve the quality of produced parts, especially those with complex geometries. More specifically, the complex designs produced through traditional manufacturing have structural flaws in regions where conventional machines cannot fill with a sufficient amount of materials such as joints due to low resolution of these machines, which consequently reduces the mechanical performance of the produced part. Hence, the AM machines can be implemented to effectively assemble the complex geometry through printing joints between elements composing lattice. The mechanical performance of the assembled lattice structure is profoundly affected by the joint connections, especially the shape and material property of the connection [130]. In order to overcome the problem of using joints in truss lattice, the PBF processes can be used to replace the traditional concept of beam element with thin sheets to produce shell lattice structure. For example, smooth shell structures characterized with Face Centered Cubic symmetry can be retrieved through locally smoothing the geometry of thin-walled octet trusses. The obtained surface is quite similar to a TPMS, as demonstrated in figure 6.

The TMPS-like structure exhibits noticeable anisotropy in both large and small strain responses, with loading-direction dependent variations in the stiffness of higher than 100%. The relative density with values ranges between 1%–50%. The shell lattices usually show a higher mechanical performance relative to truss

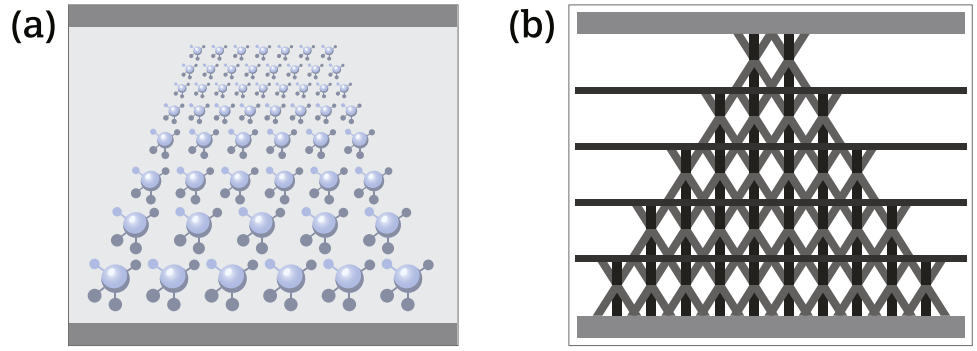

Figure 7. Functionally graded materials of (a) solid and (b) cellular materials achieved by FGAM.

lattices of equal density. The shell lattices outperform octet trusses in terms of plastic dissipation. The good weight-specific mechanical aspects noticed for high relative densities besides the absence of discrete joints qualify the isotropic and anisotropic shell-lattices as a strong candidate for hierarchical designs. Furthermore, their open structure enables the shell lattices to be manufactured using a liquid bath and PBF printing methods [93].

Lattice structures fabricated by PBF processes can emulate the physical and mechanical properties of different types of foams by making proper alterations on their material compositions and/or complex designs. The struts of specific lattice design can be fabricated from composite materials reinforced with high strength particles, which significantly increases the overall stiffness of the structure to surpass the value of its standard foam counterpart. For instance, the auxetic foams that contain highly porous TPU exhibit an effective behavior of enduring substantial volume reduction upon the application of cyclic compressive loading. This load absorption behavior can be emulated through a group of 3D synthetic meta-materials through Buckli-crystals composing of an array of elastic spherical shells with periodical lattice patterns fabricated by SLS [99]. The energy absorption capability of additively manufactured nickel Super Alloy (Inconel) 718 is highly sensitive to stress-strain curves in addition to material density. This material is fabricated using the DMLS process, and it acts like open-cell foams in the existence of high porosity. This material can be embedded in the structural parts containing areas exposed to lower stresses relative to the rest of the structure [97].

The metallic powders could be the only raw materials that can be used in fabricating 3D printed parts with controlled porosity. Different sintering and building parameters can be set to modify the porous properties of the final metallic object. The elongation and maximum strength are increased with sintered density, but the effect is varied for each type of powder. Particle size controls both efficiency of sintering operation and final pore size, which considerably affects the mechanical strength of the printed part. The shape of the particle influences the particle packing density and the ultimate open porosity range that can be attained after sintering. Sintering time and temperature (the sintering profile) determine the pore aspects of the fabricated part [94, 131].

The AM is utilized in manufacturing topologically designed porous metallic bio-materials with an ideal bio-degradation profile providing a unique combination of properties appropriate for bone regeneration. These include bone-mimicking mechanical properties, complete, interconnected porous structure, and an option for fully regenerating bony defects [84, 132]. The biodegradation profile determines the relationship between weight losses of a porous sample due to the corrosion effect of body fluid and the time duration needed to achieve the full biodegradation of the sample within 1-2 years. The rate of weight loss of the engineered porous sample is directly affected by the topological design and the degree of porosity since the highly porous structures have a faster weight loss rate relative to ones with a smaller amount of porosity [36].

6.2. Achieving balanced strength and toughness properties through FGAM

The FGAM is defined as a layer-by-layer manufacturing process that in gradation way changes the material organization within a component to obtain the desired function. The FGAM forms a radical change from contour modeling to performance modeling through acquiring performance-driven functionality built directly in the material structure. The FGAM technique can impart local properties as requested to custom thermal, electrical, and mechanical properties within the same part. Furthermore, FGAM can strategically manage the porosity and density of the composition or can combine unique materials to create a seamless monolithic structure. For functionally graded materials processed through ME based AM, the size of gaps among filaments, and the deposition directions of each lamination are the critical manufacturing parameters that directly affect the mechanical properties of these materials. At the same time, the powder delivery technique is the main factor

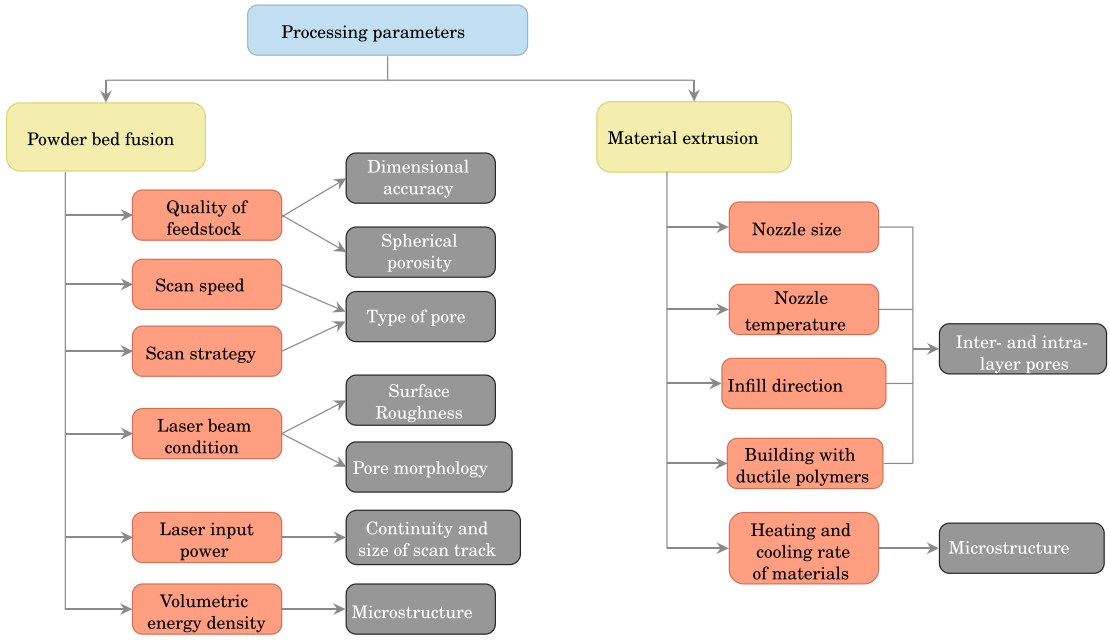

Figure 8. The effect of processing parameters on morphological aspects of materials processed by PBF and ME.

that affects the mechanical performance of complex objects with spatially varied mechanical aspects produced by PBF based AM [133, 134].

The functionally graded pores and unit cells attained through AM can be used to tune the strength and toughness properties by changing the structure of bulk and cellular materials, as demonstrated in figure 7. The fracture toughness of bulk materials can be effectively managed through introducing air pores arranged into specific shapes while varying the number and dimensions of the unit cell significantly affects weight, strength, and stiffness properties of lattice structures. The functionally graded porosity in the lattice structure can be defined through using finite element meshes to create the tessellation of the volume into a series of tetrahedrons whose edges represent the struts of the lattice [135].

The FGAM technique finds a wide variety of practical applications, such as using it to design materials with high toughness and strength properties, which form the basis of impact loading' absorbers. Furthermore, the FGAM is expected to play a vital role in fabricating lattice structures for using them in liquid cooling based heat exchangers. Also, these heat exchangers require structural performances like small thermal deformation and high stiffness [85, 136]. The functionally graded of pores can be implemented as a crucial tool for modifying the bio-degradation behavior of additively manufactured porous metallic biomaterials. SLM process is used to fabricate functionally graded biodegradable porous unit cells from pure iron powder. The topological design with functionally graded unit cells controls the mass transport properties, biodegradation behavior, and fluid flow [36].

7. The improvement of porosity through processing parameters

The basic understanding of the effect of process parameters on the microstructural evolution, and subsequently, mechanical properties of additive manufactured materials is crucial to the performance assessment of printed parts in service [137, 138]. This understanding can be developed through micromechanical modeling, which can link the processing parameters with material properties of printed parts [139, 140]. However, the accuracy of micro-mechanical modeling predictions depends on the quality of input data received through the porosity measuring technique, which is directly affected by this technique's ability to determine the distributions and forms of pores in the microstructure of the printed part. In order to improve the quality of 3D printed components, the connection between processing structure-property-performance (PSPP) should be realized. Based on the PSPP framework, the primary processing parameters and scan strategy are critical factors that affect the porosity content in the AM fabricated parts. The porosity generated by altering the processing parameters and scan strategy, primarily influences the fatigue life of the AM processed objects besides their stiffness and tensile strength properties [119]. The printing conditions of temperature and pressure inside the printer chamber can be controlled since the vast majority of AM equipment has an enclosed chamber, as they are essential for obtaining the ideal mechanical properties of the part. For instance, printing the polymeric

Table 2. The effect of processing parameters on properties of AM processed materials.

Material	AM process	Processing parameter	Affected properties	Reference
Inconel 718 alloy	SLM	Laser power	Controlling keyholes and subsurface porosity	[142]
Magnesium alloy (Mg-Ca)	SLM	Laser energy input (VED = 875–1000 J mm^{-3})	Enhanced compression performance	[143]
PA12	SLS	Elevated deposition	Reduced thermo-mechanical	[144]
ABS	FDM	temperature	creep properties	
Nylon	FDM	Layer thickness	Slight effect on stiffness and strength	[145]
HDPE	FFF	Gradient of extrusion rate	Improved surface roughness	[146]
CCF/PLA	FDM printer with external extruder	Surface treatment of CCF with PVA	The tensile and bending strengths are improved	[147]
CF/PLA	FDM printer	Nozzle temperature (230 °C) and infill orientation [0,15,−15]	The tensile properties are maximized	[148]
CF/ABS	FDM	Process additive of grape seed oil acts as a lubricant	The tensile modulus and strength are increased	[149]
CCF reinforced chopped fiber/nylon composite	FFF with two filament extruders	Increasing packing density of CCF and deposition temperature	Improved reinforcing efficiency of CCF	[150]
Nylon/ fiberglass composite	CFF	Fiber content	The mechanical strength is improved	[151]
5% short CF/PLA	FFF	Print speed = 20 mm s^{-1} and print temperature = 220 °C	The adhesive strength at fiber-matrix interface	[26]
5 wt.% short CF/PLA	FFF	Square shaped nozzle	Improved fracture toughness	[152]

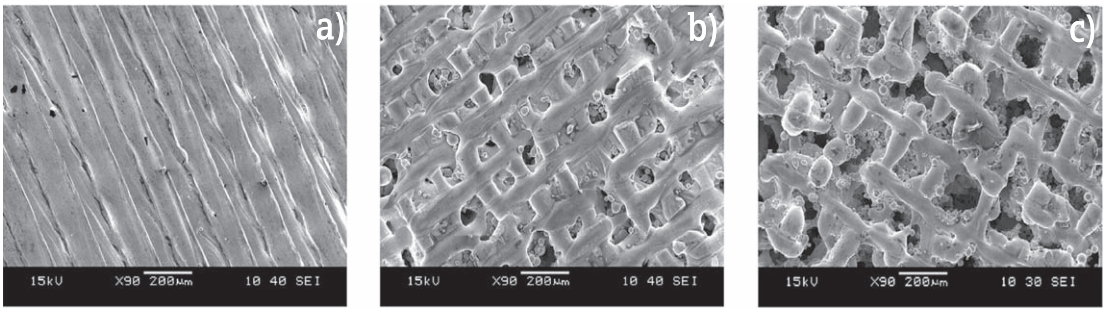

Figure 9. The quantity of un-melted powder is significantly increased when the scan strategy (high scan speed/low laser power) is modified to lower density builds: (a) 8.05 ; (b) 6.65 ; (c) 5.38 g cm^{-3}. Reprinted from [97], copyright (2017), with permission from Elsevier.

Figure 10. Optical metallographic image of nickel 718 alloys built along *Z*-axis. The scanning tracks of the laser beam are evident in the three planes. Reprinted from [154], copyright (2018), with permission from Elsevier.

components under low-pressure printing circumstances reduces porosity in their structures due to the decreased amount of oxygen entrapped in the printed structure, which increases UTS and elongation at break, and improves the bonding among the deposited layers [141].

The processing parameters of PBF and ME processes significantly affect the morphological, physical, and mechanical properties of the fabricated parts. Figure 8 summarizes the most critical parameters that have a large effect on the morphological aspects of AM processed materials classified according to the three-dimensional printing technology. Furthermore, table 2 clarifies the effect of processing parameters on the physical and mechanical properties of the materials fabricated by PBF and ME technologies.

In the SLM process, using high scan speed or low laser beam power causes insufficient melting of the powder or large space between every line and its neighbor, leading to the formation of gaps. The scan speed of laser dominates the type of pore formed and affecting the energy density transmitted to the material through the AM process. At high scan speeds, quick solidification takes place without completely filling the cavity, producing void. Thus, the relative density of the printed objects is inversely proportional to the scan speed, as demonstrated in figure 9 [97].

To minimize the voids formed at high scan speeds and increase the density of the part, the scanning strategy is the crucial parameter through scanning every layer twice with various laser powers per scan. The laser power governs the quantity of energy transmitted to the irradiated substance.Therefore, for the complete melting of highly-reflective materials such as aluminum alloys, high laser power is needed. Moreover, the laser power controls the continuity and size of a scan track, influencing the structural integrity of the parts. Similar to laser power, the scan speed governs the melting and solidification rates. By decreasing the scan speed, the irradiated spot is maintained longer and needs more time to solidify and influence the microstructure and control the track size [111, 153].

The VED of the laser beam is directly correlated with SLM parameters (scan speed, laser power, and distance between scan lines). With increasing VED values, the density of the produced part increases (porosity is reduced) until reaching a specific limit corresponding to melting.Beyond this limit, the quality of the part begins to decline because of thermal stresses and induced residual stresses. Furthermore, the VED has a considerable effect on the columnar-dendritic microstructure of SLM processed metals such as nickel 718 alloy, as it can be inferred from figure 10 [154, 155]. However, optimizing the processing parameters based on energy density is not technically feasible. Hence, an optimized processing window is needed to be set in terms of scan speed and laser power parameters [156].

The laser power and scan speed considerably affect the open porosity of parts fabricated by SLS. By regulating these two parameters, the maximum variation in open porosity can be attained [157]. The laser conditions of the fiber laser can also significantly contrast in the surface roughness and morphology of porous structures printed by the SLS process, which is attributed to the change in energy density irradiated to the powder's surface [158]. Highly dense printed parts can be attained even if high scan speed and low energy density parameters are used during the printing process by changing the heating depth and reducing the hatch spacing, facilitating the re-melting of the solidified region [159].

The poor optimization of processing parameters leads to the formation of keyholes in the printed structure. The ratio of hatch spacing to melt pool width can be critical. The minimal ratio can cause key-holing porosity, even though the scan speed and laser power values are not capable of inducing key-holing. On the other hand, the substantial ratio can promote the formation of a lack of fusion porosity because of fluctuations in the dimensions of the melt pool [160]. Increasing the space between contour scan tracks and hatch scan tracks promotes the formation of close to surface porosity in metallic parts processed by laser PBF. Additionally, the lack of fusion pores are appeared due to poor hatch overlap, and the distribution of these pores is influenced by large layer height spacing [161]. The spherical shaped internal porosity is formed in the structure of parts fabricated by PBF processes due to the gas atomization process used for producing powders [162]. Thus, choosing the appropriate material for the feedstock has a significant effect on the dimensional accuracy and porosity formation [163]. The pre-heating of the powder bed, along with optimized processing parameters, can effectively deter the formation of a crack in alloys fabricated by laser PBF with an extensive solidification range such as AA6061 [164]. Besides, the high powder mass feed rate significantly improves the dimensional accuracy of the printed part. Thus, porosity and layer thickness considerably depend on this feed rate at fixed laser input power. At a higher powder feed rate, the level of porosity can be improved with an increasing power input of the laser beam. The higher powder mass feed rate leads to more significant porosity, but the potential of real layer thickness formation is improved [159].

The family of ME technology contains printing machines with a wide variety of nozzle and bead sizes like FDM, BAAM, and LSAM. The last two machines can form beads with a 6–21 mm bead width and a 4–5 mm bead height. In filament extrusion-based AM, choosing wide nozzle sizes of 0.40 to 21 mm is considered an appropriate solution for avoiding stacked void areas, and it minimizes the content of pores in every layer. Hence, by reducing a bead width, the pore content is minimized, and thus, the strength is enhanced since there is more material processed in a unit volume [165]. Setting the nozzle temperature to insufficient values needed for smooth extrusion of filaments will induce the formation of intra and interlaminar voids in FFF-fabricated parts [107, 166]. Moreover, the infill direction, heating, and cooling rates of processed materials, in addition to nozzle temperature, significantly affect the porosity and subsequent physical properties such as toughness, strength, stiffness, and ductility of ME processed fiber composites [167]. The infill direction has a higher effect on porosity and associated mechanical properties in terms of anisotropy compared to scan speed [77]. Nevertheless, in extrusion-based AM, the infill direction does not play a key role in affecting UTS values if the processing parameters are set to minimize the infill tangency voids, surface edges, and elongated voids [168].

The porosity formed in FDM fabricated part is highly affected by the ductility of the raw materials since the brittle laminated material has a higher amount of inter- and intra- pores relative to ductile one. Therefore, using layers of ductile polymers such as ABS in the laminates of polymeric composite processed by FDM is considered an effective way of improving the ductility of the printed structure if processing parameters of moderate layer height, high clad ratio, and low printing speed are maintained. The composites manufactured using these parameters' settings could possess high toughness and strength properties at the same time in addition to reduced porosity content among composite layers [169].

8. Post treatments of porous defects

The processes of AM are unable to manufacture part with acceptable surface roughness and mechanical properties that meet the requirements of most structural applications. Hence, after object building, some post-processing treatments are needed. These include processes that aid in enhancing the surface quality by using, for

example, finer powder, heat treatments to release the residual stresses emerged from the thermal stress and to close the keyhole defects, in addition to the HIP treatment that mitigates the porosity and enhance the microstructure [170–172]. Besides the aforementioned physical treatments, chemical-based post-treatments can be used to modify the chemical structure of the printed part containing pores to reduce their content and to improve its surface roughness along with other morphological aspects. More details about the post-treatments used on porosity reduction are discussed in the following subsections.

8.1. Post heat treatment

The post-processing based on heat treatments such as laser polishing and post sintering treatment contributes effectively in decreasing the surface's excessive roughness and closing the internal pores in 3D printed parts, especially those with sensitive structures which cannot be treated with pressure loads such as lattices and highly porous scaffolds. The stress-relieving heat treatment has higher effectiveness on reducing the porosity of 3D printed lattice structures (especially at nodes) fabricated from nickel alloy 718 compared to HIP processing. Furthermore, this heat treatment improves the quasi-static and dynamic flow stress after yielding [173]. The post-heat treatment can be combined with other treatment methods used for post-processing of conventionally manufactured materials such as rolling, in addition to surface finishing treatments of sandblasting, roto-polishing, and ultrasonic striking [83, 174]. The post sintering treatment contributes to fusing particles together, removing the pores, and considerably enhancing the mechanical properties of parts produced by SLS [20]. The heat treatment increases the mechanical strength of nickel alloy 718 processed through EBM, but it does not eliminate its anisotropy behavior [175]. After treating LB-PBF fabricated AerMet100 steels plate with a tempering temperature of 1300 °C, the tensile mechanical properties and ductility are considerably improved. This enhancement is attributed to tremendously strong strain strengthening capability attained through dispersive precipitation of M2C carbides. Due to the significant size reduction of carbide achieved with increasing tempering temperatures, the large porosities are rarely noticed in the fracture surfaces of the tempered specimens [176]. Nevertheless, by increasing the tempering temperature of post heat treatment from 505 °C to 515 °C, the fracture toughness of LB-PBF processed AF1410 steel is reduced due to the effect of an increasing number of reversed austenite and coarsened carbides which promoting the formation of pore nucleation [177]. Furthermore, a solution, quenching, and aging heat treatment conducted on the AlSi10Mg object, which is fabricated through DMLS, decreases its UTS and elongation properties without affecting the YS at a moderate increase of porosity. The higher tensile mechanical properties of the as-deposited sample are justified to its finer microstructure compared to heat-treated one [178].

If typical polishing parameters are implemented, the laser polishing technology enhances the surface quality of the Al/PLA composite fabricated through FDM. The polished and re-melted surfaces of the samples lead to enhancements in Young's modulus and tensile strength. This improvement is attributed to the theory that the laser heat improves the interfacial adhesion at Al/PLA interface and reduces the content of internal porosity located near to surface. The melted surface material flows from the peak toward unfilled spaces near them, eliminating many material flaws. After removing the laser beam, the densification of the structure is increased since the melted materials re-bond together after cooling [106].

8.2. Post pressure and heat treatment

HIP post-treatment is used for improving the densification characteristic of AM fabricated part through applying iso-static gas pressure and elevated temperature on the printed structure. In some classes of additively manufactured soft materials such as FFF-processed silicone, the elastomer can be processed without using gas pressure. The formation of pores in each layer of silicone can be prevented through using the compressing pressure-induced due to layer deposition [179]. The HIP treatment is very effective in closing the functional pores in PBF fabricated parts. For instance, HIP treatment homogenizes the structure of Ti-6Al-4V alloy processed by PBF independent of location and orientation on the build plate [180]. HIP treated samples, which are fabricated from Ti-6Al-4V processed by direct laser deposition, exhibit superior densification and tensile strength properties relative to untreated specimens. However, the elevated temperatures experienced during the HIP process lead to an increase in the thickness of the alpha-platelet of Ti-6Al-4V, which decreases the strength of the material [21, 181].

The heat processing in HIP post-treatment is used to enhance the mechanical properties and microstructure of Inconel 718. High pressure up to 200 MPa and temperature up to 1280 °C cause plastic deformation and diffusion and thus seal the internal voids. However, the HIP is incapable of closing pores in the direct vicinity of the build surface or pores enclosing gas [23]. The oxidation resistance of nickel alloy 718 processed by SLM is enhanced after applying HIP treatment at high temperature (900, 1000 °C), which is justified to the high density of the HIP treated sample and controlling of microstructural variations at the grain boundaries [182]. The HIP treatment reduces the porosity content of SLM fabricated AlSi10Mg specimen by 44% and 65% for vertical and

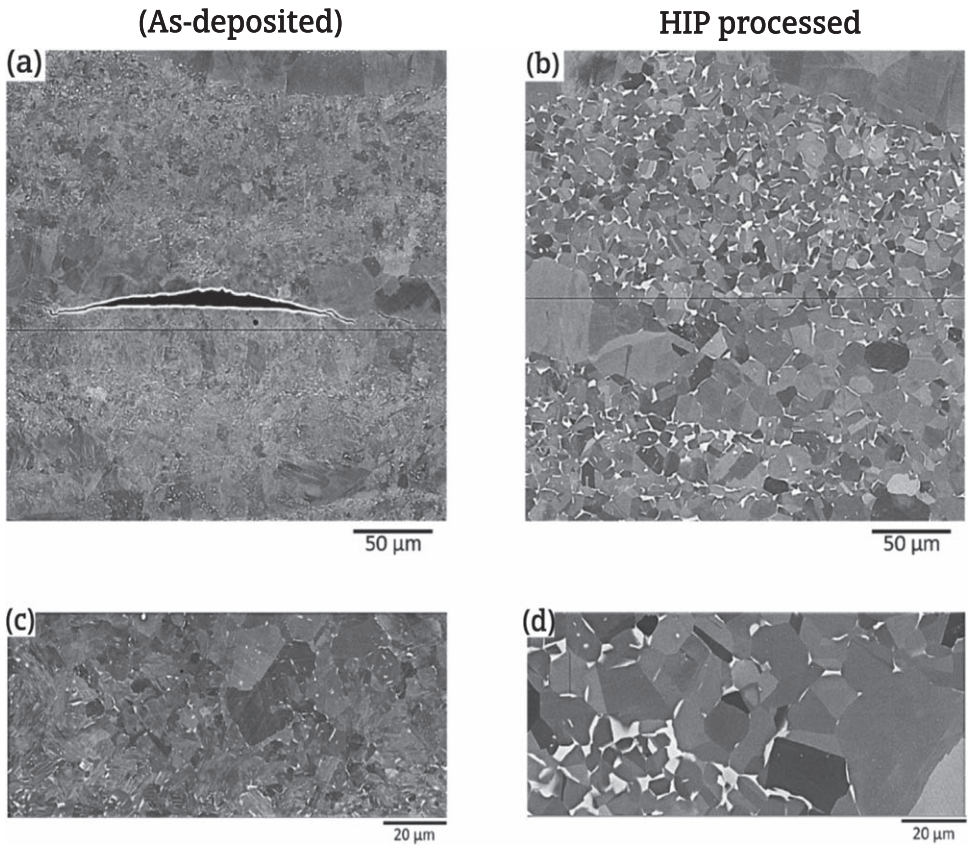

Figure 11. Images of as-built and HIP processed material showing the drastic microstructure spatial heterogeneity prior to and after HIP processing under identical magnification (a)–(b) and reduced magnification (c)–(d). Reprinted from [185], copyright (2017), with permission from Elsevier.

horizontal layering depositions, respectively. The fatigue life of this sample is directly affected by the presence of pancakes like voids normal to the loading direction. Thus it is better to fabricate specimens transverse to the highest fatigue loads. The pancake-shaped pores considerably reduce the fatigue life of vertical layering deposited specimens for which the plane of the pores is transverse to the fatigue load, compared to those fabricated horizontally for which the pores are edge-on to the fatigue load [183].

Direct laser fabrication is used to fabricate three high entropy alloys (HEAs) based on the AlxCoCrFeNi alloy system with various aluminum molar fractions (x) of 0.3, 0.6, and 0.85. The HIP treatment increases the specimen density by reducing the number of large pores with sizes larger than 5.0 μm in the as-built alloys. Moreover, the HIP induces chemical homogenization and microstructural coarsening leading to general enhancement in the mechanical properties of face-centered cubic HEA with $x = 0.3$. For alloy with $x = 0.85$, the HIP considerably reduces its ductility due to the formation of σ-phase precipitates and coarsening of the microstructure [184]. Based on scan results of μ-CT, in-homogeneous microstructures have appeared in both as-built, and HIP treated γ-TiAl material processed by electron beam based PBF. Processing this material with HIP decreases its YS as well as the amount of scattering in mechanical properties. HIP treatment is efficient in decreasing or even eliminating the manufacturing-induced flaws but does not considerably alter the grain size or decrease the microstructural heterogeneities, as demonstrated in figure 11. However, some residual cracks are detected even after the application of HIP processing. The homogenization of microstructure will need HIP coupled with heat treatment in the single-phase alpha regime, which could lead to coarse-grain, fully lamellar microstructure. The microstructure change is consistent with strength reduction noticed on HIP treated material and increase in notch toughness [185].

The HIP post-treatment can be combined with other conventional treatments such as sandblasting and light chemical etching in order to enhance the biological response and damage tolerance of Ti-6Al-4V lattice meta-bio-materials printed by SLM process. The combination of surface engineering and microstructural design induced by sandblasting and HIP, respectively, enables to increase the endurance limit of Ti6Al4V by two folds under fatigue loads. The HIP processing drastically reduced the internal porosity and changed the microstructure's behavior to be a more ductile mixture of $\alpha + \beta$ phases [82].

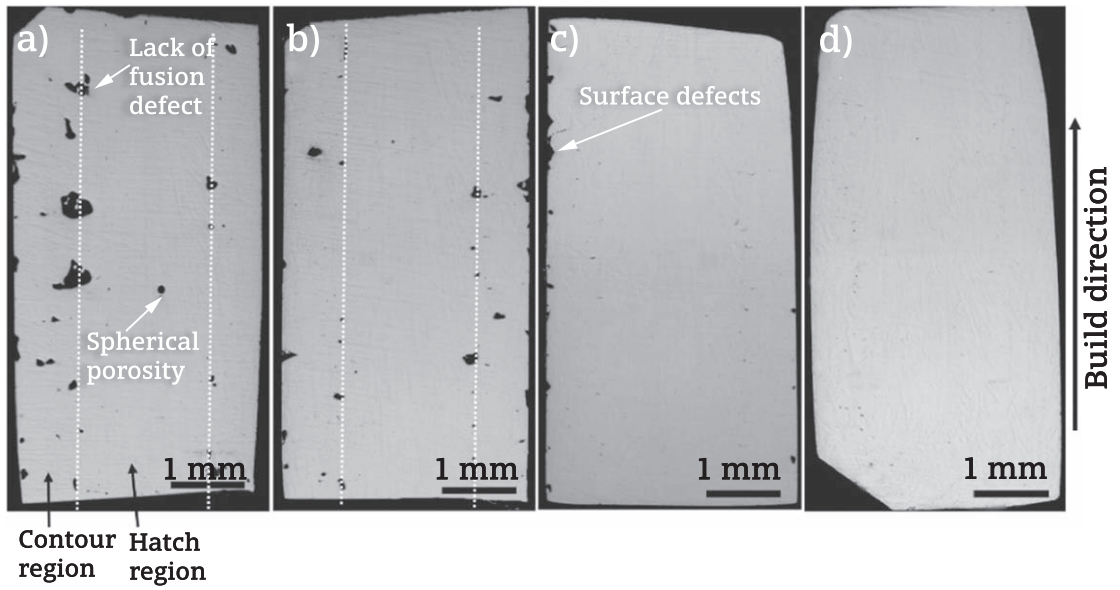

Figure 12. Cross-sections of nickel 718 alloy retrieved through light optical microscopy: (a) as-deposited, (b) HT, (c) HIP, and (d) HIP-HT. Reprinted from [189], copyright (2019), with permission from Elsevier.

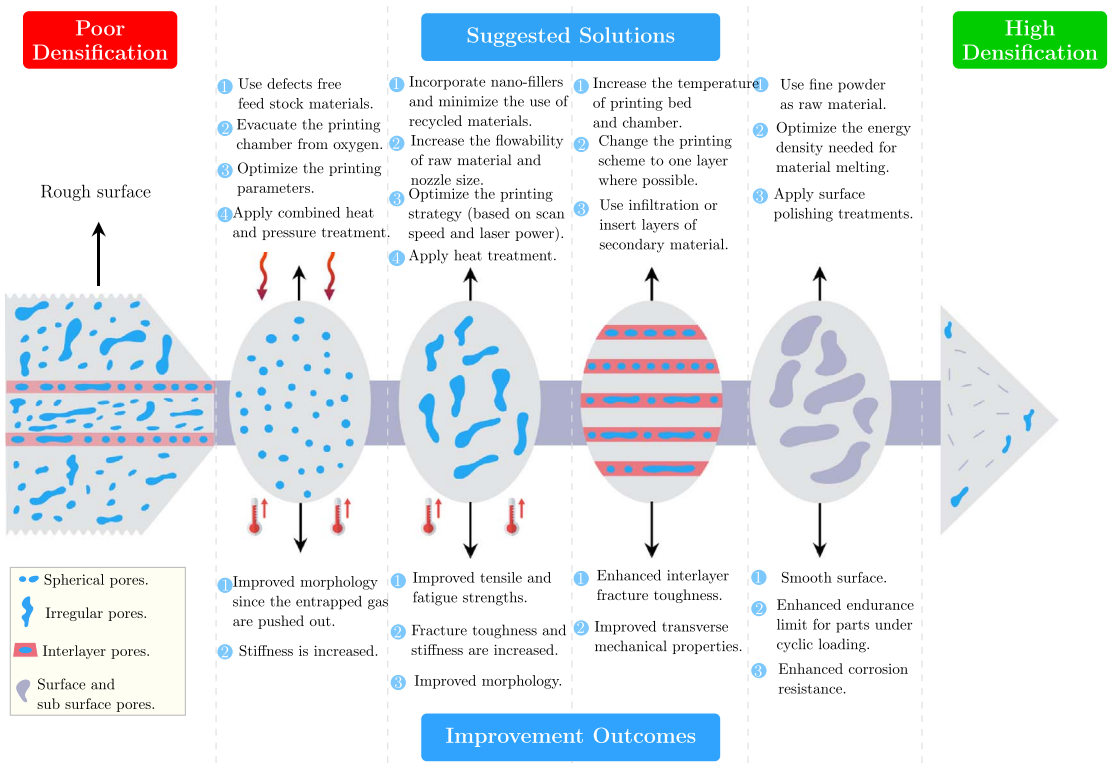

Figure 13. Optimizing the mechanical performance of AM processed materials.

The fatigue strength of the AM fabricated objects is significantly affected by the surface finish parameter. Therefore, shot peening is used to improve the resistance of materials and parts toward stress corrosion cracking and fatigue. This treatment process has undesirable effects on the machined parts when the parameters (such as shot speed, time of exposure to shot peening, and hardness of the shot) are not set correctly. The residual compressing stresses are generated in the treated part due to the plastic deformation occurs at its surface upon the application of intensive shot peening treatment [186]. Initially, increasing the peening intensity leads to noticeable enhancement in fatigue life at high cycle plain fatigue, but with further peening, the fatigue aspects fallback [187]. The combination of shot peening and HIP improves the monotonic stress-strain behavior of SLM

processed Ti-6Al-4V due to the elimination of different types of process-induced defects, including porosity. However, under cyclic loading and after applying HIP treatment to SLM processed material, several small flaws remain in the treated area leading to cumulative damage without considerable macro crack growth starting from more substantial defects [188]. For oxidation exposure at 850 °C, the combined thermal post-treatment of HIP coupled with heat treatment (HIP-HT) considerably enhance the oxidation properties of nickel alloy 718 fabricated through electron beam PBF (EB-PBF). Due to its efficient capability to reduce the size of irregular pores and to close the circular pores, it leads to a more homogenized and tailored microstructure as it can be inferred from figure 12 [189]. The HIP treatment promotes the reduction of both lacks of fusion flaws and porosity, introducing effective improvements in mechanical properties of laser PBF processed H13 tool steel. HIP followed by heat treatment, leads to the highest ductility and strength and the minimal scatter in elongation to fracture because of porosity reduction [190].

Components fabricated by metal PBF in which the component bed is below the annealing temperature of the alloy will probably form residual thermal stresses through processing. The application of heat treatment on components, while they are attached to the build platform, is necessary to avoid geometric distortion from these stresses when the fabricated pieces are removed from the build platform. The HIP and solution annealing are proved their effectiveness in reducing porosity despite the associated change on the microstructure of treated parts. According to condition T6 treatment used for metallic parts fabricated by PBF, they should have a solution heat treatment at a temperature of 530 $\pm$ 6 °C for a minimum duration of 6 hours and then quenching in glycol or water followed by aging at 160 $\pm$ 6 °C for a minimum duration of 360 minutes [191]. T6 heat treatment and HIP processing are used to improve the properties and microstructure of an AlSi10Mg alloy, which is additively manufactured with sub-optimal printing parameters. A significant lack of fusion flaws aligned normal to the loading axis (or in the same direction of the fracture plane) is very critical. However, when aligned favorably (normal to crack propagation direction), the alloy is still able to attain comparable ductility and strength to the results mentioned in literature for laser PBF processed AlSi10Mg alloys. The HIP processing is unable to close the large flaws (potentially due to trapped Ar gas), leading to low improvement of fatigue performance of sample with combined treatment of HIP and T6. The microstructure processed solely with HIP exhibit good toughness and high ductility [192].

8.3. Post chemical treatment

Most chemical post-treatments are used to improve the surface finish and decrease the porosity of AM processed materials, enhancing their fatigue strength and other physical properties such as corrosion and wear resistance. For instance, the strain to failure, strength, and volumetric energy of Kagome truss unit cell, which is manufactured from ABS and processed by FDM printer, are increased upon the application of acetone treatment with a concentration of 90% (v/v) for 5.0 minutes due to the reduced surface roughness. Usually, the rough surfaces facilitate the initiation of surface cracks, and these begin to propagate under applied load [105]. The entanglement and diffusion of neighboring FDM printed layers are improved after blending low molecular weight (LMW) polymer with an identical but high molecular weight polymer (synthesizing the printing filaments). Upon the incorporation of only 3mol.% of each LMW additive, the maximum stress is increased from 15% to 100% for specimens manufactured in the transverse orientation. This improvement is attributed to the capability of linear LMW additives of adequate length on entangling and diffusing with neighboring matrix leading to enhanced interlayer interface [193]. Poly(styrene-maleic anhydride) (SMA) compatibilizer is used to improve the interfacial adhesion between beads and subsequent anisotropy ratio and mechanical properties of ABS/polyamide (PA) blend processed by FFF printer. The flexural test results exhibit 77% enhancement in the anisotropy ratio of the strength, 55% enhancement in the anisotropy ratio of Charpy impact strength, and 62% enhancement in the anisotropy ratio of modulus compared to referenced values of PA. The anisotropy ratio is defined as (property evaluated along the *z*-axis)/(property measured along the *x*-axis). This ratio is used to represent bead to bead adhesive strength [194].

The properties and quality of 3D printed NFRCs depend on many factors, such as properties of build materials, the temperature of the printing chamber, nozzle diameter, deposition speed, width of the deposited road, filament feed rate, and temperature of deposition head. When the adhesion at the fiber/matrix interface is insufficiently strong, the content of voids is increased with increasing loading of fibers. Furthermore, the loading of voids is increased with print width (specimen size) due to loss of deposit temperature through the AM of large specimens with more significant deposition paths. Components fabricated from PLA reinforced with recycled wood fiber at 15.2 wt.% exhibit considerable loading of porosity, which can be controlled through suitable optimization of FFF printing parameters and feedstock preparation. The impact of porosity can be efficiently mitigated through the orientation of fibers in the same direction of the applied load. The voids content in FFF-processed NFRCs can be reduced by incorporating thermally expandable microspheres (2.0 wt.%) in the polymer matrix structure. Through post-manufacturing thermal treatment, the micro-spheres within polymer

expand and generate compressing stress on the pores, thus seal them [195]. In order to attain the desired functional and mechanical performance in NFRC, it is crucial to control, length and weight fraction of fibers in achieving the required reinforcing effect, the distribution and orientation of fibers within the hosting matrix, bonding strength at fiber/matrix interface, and structural flaws such as porosity. Chemical treatment methods are used to improve the bonding strength at the fiber/matrix interface for NFRC processed through the FFF printer. The flow rate and ease of processing of NFRCs can be enhanced through (i) altering the chemical structure of hosting polymer through incorporating compatibilizing agents, and (ii) surface modification of fibers [196, 197].

Nano and micro inclusions with a high degree of compatibility with filaments of ME based printing machines can be used to considerably improve the ease of extrusion flow along with their reinforcing effect on increasing the stiffness and strength of printed parts. For instance, The IF-WS2 nanoparticles are used to improve the ease of flow of PEEK processed through the FFF printer without affecting its thermal and mechanical properties. This behavior is attributed to IF-WS2 nano-fillers that act as both lubricating and reinforcing agents [198]. The Si nanoparticles are used to improve UTS, Young's modulus, and elongation at break of PMMA filaments of the FFF printer. These enhancements are attributed to hydrogen bonding interaction between hydroxyl groups on the surface of inorganic Si particles and carbonyl groups of PMMA. These interfacial entanglements mitigate chain mobility at the surface, which improves the stress transfer from PMMA to Si additive [199]. The chopped thin fibers with a considerable length to diameter ratio introduce higher porosity content in FDM printed fibrous plastic composite relative to nanoparticles. However, the tensile properties of chopped fiber/plastic composite are higher than those of particle reinforced composite due to wider interaction area among the neighboring layers, leading to higher bonding strength relative to particles reinforced composite materials [200].

9. Conclusion

The random air voids defects have a significant adverse impact on the physical and mechanical properties of the materials processed by powder bed fusion and material extrusion since these technologies depend on solid raw materials to additively manufacturing parts. The pores that emerged from AM are distributed into three critical locations in the structure of additively manufactured parts: in the bulk material, between deposited layers, and at the fiber/matrix interface region for fiber composite materials processed by AM. The interlayer generated pores have a critical effect on bond strength. They are essential for the mechanical performance of printed structures when the load is applied in the transverse direction normal to the printed layers.

Powder bed fusion induced pores have two main shapes: spherical pores formed due to the gas entrapped in the powder during the powder atomization process, while the irregular pores (keyholes) are generated due to the insufficient optimization of processing parameters, such as laser beam power and scan speed. The irregular pores have a higher undesirable effect on many material properties than spherical pores, such as stiffness, strength, and fatigue life, since these pores promote the initiation of damage within the structure of the printed material. The engineered porosity designed by the mean of AM processes can increase the ductility of the printed part through trading off with strength and stiffness properties. The keyhole defects can be effectively treated by combining HIP and heat post-treatments. The HIP is efficient in closing spherical pores unless they are filled with gas, which resists the compressing loads applied during this treatment. The most recent solutions, which can be useful in treating all types of air pores, are summarized in figure 13, along with their improving effect on the mechanical properties of AM processed materials. The AM technology can play a crucial role in generating new classes of smart materials with improved strength and toughness properties, uniquely if this technology is integrated with traditional composite manufacturing methods. There is a need to develop new porosity measuring equipment that can detect and quantify porous defects at different scales from micro to macro levels with acceptable accuracy and a reasonable amount of processing data. Moreover, there is a limited number of studies investigate the effect of porous flaws in terms of porosity location and shapes on the fatigue properties of parts fabricated by ME processes. Hence, further research is needed to address this challenge quantitatively and qualitatively in addition to developing new treatment technologies that can improve the resistance of the part against fatigue cracks.

Acknowledgments

The research fund granted by German Academic Exchange Service (DAAD) for the purpose of accomplishing this research is acknowledged and appreciated.

ORCID iDs

Ahmad Y Al-Maharma https://orcid.org/0000-0003-1127-734X
Sandeep P Patil https://orcid.org/0000-0003-3980-6995
Bernd Markert https://orcid.org/0000-0001-7893-6229

References

[1] Guo N and Leu M 2013 *Front. Mech. Eng.* **8** 215–43
[2] Labonnote N, Rønnquist A, Manum B and Rüther P 2016 *Autom. Constr.* **72** 347–66
[3] Rajaguru K, Karthikeyan T and Vijayan V 2020 *Mater. Today Proceed* **21** 628–33
[4] Daminabo S, Goel S, Grammatikos S, Nezhad H and Thakur V 2020 *Mater. Today Chem* **16** 100248
[5] Parandoush P and Lin D 2017 *Compos. Struct.* **182** 36–53
[6] ASTM 2014 *Standard Guide for Characterizing Properties of Metal Powders Used for Additive Manufacturing Processes* URL www.astm.org
[7] ASTM 2014 *Standard Specification for Additive Manufacturing Titanium-6 Aluminum-4 Vanadium with Powder Bed Fusion* URL www.astm.org
[8] Palanikumar K, Mudhukrishnan M and Prabha P S 2020 *Curr. Opin. Chem. Eng.* **28** 51–9
[9] Brenken B, Barocio E, Favaloro A, Kunc V and Pipes R 2018 *Addit Manuf* **21** 1–16
[10] Singh S, Singh G, Prakash C and Ramakrishna S 2020 *J. Manuf. Processes* **55** 288–306
[11] ASTM 2015 *Standard Test Method for Apparent Porosity in Cemented Carbides* URL www.astm.org
[12] ASTM 2019 *Standard Terminology of Advanced Ceramics* URL www.astm.org
[13] Hofstätter T, Pedersen D, Tosello G and Hansen H 2017 *J. Reinf. Plast. Compos.* **36** 1061–73
[14] Moustafa A, Dinwiddie R, Pawlowski A, Splitter D, Shyam A and Cordero Z 2018 *Addit Manuf* **22** 223–9
[15] Türk D A, Einarsson H, Lecomte C and Meboldt M 2018 *Prod. Eng.* **12** 203–13
[16] Kumar A Y, Wang J, Bai Y, Huxtable S and Williams C 2019 *Mater. Des.* **182** 108001
[17] Kong D, Ni X, Dong C, Zhang L, Yao J, Man C, Wang L, Xiao K and Li X 2019 *Constr Build Mater* **221** 720–9
[18] Thompson M *et al* 2016 *CIRP Ann Manuf Technol* **65** 737–60
[19] Martínez-Frutos J, Allaire G, Dapogny C and Periago F 2019 *Comput Methods Appl Mech Eng* **345** 1–25
[20] Dizon J, Espera A, Chen Q and Advincula R 2018 *Addit Manuf* **20** 44–67
[21] Sola A and Nouri A 2019 *J. Adv. Manuf. Process.* **1** e10021
[22] Fotovvati B, Etesami S and Asadi E 2019 *Mater. Sci. Eng.* A **760** 431–47
[23] Hosseini E and Popovich V 2019 *Addit Manuf* **30** 100877
[24] DebRoy T, Wei H, Zuback J, Mukherjee T, Elmer J, Milewski J, Beese A, Wilson-Heid A, De A and Zhang W 2018 *Prog. Mater. Sci.* **92** 112–224
[25] Plocher J and Panesar A 2019 *Mater. Des.* **183** 108164
[26] Papon E, Haque A and Mulani S 2019 *Compos. B. Eng.* **177** 107325
[27] Keleş Ö, Anderson E H, Huynh J, Gelb J, Freund J and Karakoç A 2018 *Sci. Rep.* **8** 1–12
[28] van de Werken N, Hurley J, Khanbolouki P, Sarvestani A, Tamijani A and Tehrani M 2019 *Compos. B. Eng.* **160** 684–92
[29] Blok L G, Longana M L, Yu H and Woods B K 2018 *Addit Manuf* **22** 176–86
[30] Zindani D and Kumar K 2019 *Int. J. Lightweight Mater. Manuf.* **2** 267–78
[31] Gorelik M 2017 *Int J Fatigue* **94** 168–77
[32] Tapia G and Elwany H S A 2016 *Addit Manuf* **12** 282–90
[33] Zhang B, Liu S and Shin Y 2019 *Addit Manuf* **28** 497–505
[34] Liu J, Liu C, Bai Y, Rao P, Williams C and Kong Z 2018 *IISE Trans.* **51** 109–23
[35] Carvalho M, Martins A and Santos T 2019 *Appl. Therm. Eng.* **159** 113872
[36] Li Y *et al* 2019 *Acta Biomater.* **96** 646–61
[37] Al-Ghouti M A and Da'ana D A 2020 *J. Hazard. Mater.* **393** 122383
[38] Karimi S, Yaraki M T and Karri R R 2019 *Renew. Sust. Energ. Rev.* **107** 535–53
[39] Unuabonah E I, Omorogie M O and Oladoja N A 2019 Modeling in adsorption: fundamentals and applications *Composite Nanoadsorbents* (Amsterdam: Elsevier) pp 85–118
[40] McMillan W and Teller E 1951 *J. Phys. Chem.* **55** 17–20
[41] Saevels S, Berna A Z, Lammertyn J, Di Natale C and Nicola B M 2004 *Sens. Actuators B Chem.* **101** 242–51
[42] Gibson N, Kuchenbecker P, Rasmussen K, Hodoroaba V D and Rauscher H 2020 vol-specific surface area by gas adsorption analysis with the bet method *Characterization of Nanoparticles* (Amsterdam: Elsevier) pp 265–94
[43] Sing K S 2014 Assessment of surface area by gas adsorption *Adsorption by Powders and Porous Solids* ed F Rouquerol *et al* 2nd edn (New York: Academic) pp 237–68
[44] Yurdakal S, Garlisi C, Özcan L, Bellardita M and Palmisano G 2019 (photo) catalyst characterization techniques: Adsorption isotherms and bet, sem, ftir, uv-vis, photoluminescence, and electrochemical characterizations *Heterogeneous Photocatalysis* (Amsterdam: Elsevier) pp 87–152
[45] Naderi M 2015 Surface area: Brunauer-emmett-teller (bet) *Progress in Filtration and Separation* (Amsterdam: Elsevier) pp 585–608
[46] Joshi N, Romanias M N, Riffault V and Thevenet F 2017 *Aeolian Res* **27** 35–45
[47] Zhou S, Zhang D, Wang H and Li X 2019 *Mar Pet Geol* **105** 284–92
[48] Kim F, Moylan S, Garboczi E and Slotwinski J 2017 *Addit Manuf* **17** 23–38
[49] Saâdaoui M, Khaldoun F, Adrien J, Reveron H and Chevalier J 2020 *J. Eur. Ceram. Soc.* **40** 3200–7
[50] Fieres J, Schumann P and Reinhart C 2018 *Procedia Eng.* **213** 69–78
[51] Zanini F, Sbettega E and Carmignato S 2018 *Procedia CIRP* **75** 114–8
[52] Hermanek P and Carmignato S 2017 *Precis Eng* **49** 377–87
[53] Zikmund T, Šalplachta J, Zatocilová A, Brínek A, Pantelejev L, Štepánek R, Koutný D, Paloušek D and Kaiser J 2019 *NDT E Int.* **103** 111–8
[54] Oromiehie E, Garbe U and Prusty B G 2020 *J Compos Mater* **54** 1217–31

[55] Na J and Oneida E 2018 *Addit Manuf* **24** 154–65
[56] Plessis A D, Sperling P, Beerlink A, Tshabalala L, Hoosain S, Mathe N and Roux S L 2018 *Methodsx* **5** 1102–10
[57] Goh G, Dikshit V, Nagalingam A, Goh G, Agarwala S, Sing S, Wei J and Yeong W 2018 *Mater. Des.* **137** 79–89
[58] Hinton T, Lee A and Feinberg A 2017 *Curr. Opin. Biomed. Eng.* **1** 31–7
[59] i Park S and Rosen D 2016 *Addit Manuf* **12** 265–73
[60] Lee H, Kim J H, Moon J H, Kim W W and Seo E A 2019 *Constr Build Mater.* **226** 712–20
[61] Murr L, Martinez E, Amato K, Gaytan S, Hernandez J, Ramirez D, Shindo P, Medina F and Wicker R 2012 *J. Mater. Res. Technol.* **1** 42–54
[62] Wang P, Tan X, He C, Nai M, Huang R, Tor S and Wei J 2018 *Addit Manuf* **21** 350–8
[63] Tan Z, Pang J, Kaminski J and Pepin H 2019 *Addit Manuf* **25** 286–96
[64] Montazeri M, Nassar A, Dunbar A and Rao P 2020 *IISE Trans.* **52** 500–15
[65] Choren J, Heinrich S and Silver-Thorn M 2013 *J. Mater. Sci.* **48** 5103–12
[66] Vastola G, Pei Q and Zhang Y 2018 *Addit Manuf* **22** 817–22
[67] Biswal R, Zhang X, Shamir M, Mamun A A, Awd M, Walther F and Syed A 2019 *Addit Manuf* **28** 517–27
[68] Moumen A E, Tarfaoui M and Lafdi K 2019 *Compos. B. Eng.* **171** 166–82
[69] Serdeczny M, Comminal R, Pedersen D and Spangenberg J 2019 *Addit Manuf* **28** 419–29
[70] Karakoç A, Rastogi V K, Isoaho T, Tardy B, Paltakari J and Rojas O J 2020 *Materials* **13** 422
[71] Dickson A and Dowling D 2019 *Compos. Struct.* **212** 381–8
[72] Singh A, Patil B, Hoffmann N, Saltonstall B, Doddamani M and Gupta N 2018 *JOM* **70** 303–9
[73] Jahangir M, Billah K, Lin Y, Roberson D, Wicker R and Espalin D 2019 *Addit Manuf* **28** 354–64
[74] Kumar S, Singh R, Singh T and Batish A 2019 *J. Thermoplast. Compos. Mater.* **1** 0892705719856063
[75] Dickson A, Barry J, McDonnell K and Dowling D 2017 *Addit Manuf* **16** 146–52
[76] Dickson A, Ross K A and Dowling D 2018 *Compos. Struct.* **206** 637–43
[77] Zhang W, Wu A, Sun J, Quan Z, Gu B, Sun B, Cotton C, Heider D and Chou T 2017 *Compos Sci Technol* **150** 102–10
[78] Spoerk M, Savandaiah C, Arbeiter F, Traxler G, Cardon L, Holzer C and Sapkota J 2018 *Compos. Part A Appl. Sci. Manuf.* **113** 95–104
[79] Li Y, Feng Z, Huang L, Essa K, Bilotti E, Zhang H, Peijs T and Hao L 2019 *Compos. Part A Appl. Sci. Manuf.* **124** 105483
[80] Zhang Z, Yao X and Ge P 2020 *Int. J. Mech. Sci.* **166** 105230
[81] Harooni A, Iravani M, Khajepour A, King J, Khalifa A and Gerlich A 2018 *Addit Manuf* **22** 537–47
[82] Ahmadi S *et al* 2019 *Acta Biomater.* **83** 153–66
[83] Kelly C, Evans N, Irvin C, Chapman S, Gall K and Safranski D 2019 *Mater. Sci. Eng.* C **98** 726–36
[84] Kadkhodapour J, Montazerian H, Darabi A, Anaraki A, Ahmadi S, Zadpoor A and Schmauder S 2015 *J Mech Behav Biomed Mater* **50** 180–91
[85] Dumas M, Terriault P and Brailovski V 2017 *Mater. Des.* **121** 383–92
[86] Bartolomeu F, Fonseca J, Peixinho N, Alves N, Gasik M, Silva F and Miranda G 2019 *J Mech Behav Biomed Mater* **99** 104–17
[87] Lütjering G, Williams J and Gysler A 2000 *Microstructure and Mechanical Properties of Titanium Alloys* 2 (Singapore: World Scientific) pp 1–77
[88] Cleaves H E and Hiegel J 1942 *J. Res. Natl. Bur. Standards* **28** 1471
[89] Singh B, Horsewell A and Toft P 1999 *J. Nucl. Mater.* **271** 97–101
[90] ASTM 2016 *Standard Specification for Additive Manufacturing Stainless Steel Alloy (UNS S31603) with Powder Bed Fusion* URL www.astm.org
[91] Suryawanshi J, Prashanth K and Ramamurty U 2017 *Mater. Sci. Eng.* A **696** 113–21
[92] Balijepalli S, Donnini R, Kaciulis S, Montanari R and Varone A 2013 Young's modulus profile in kolsterized aisi 316l steel *Materials Science Forum* 762 (Switzerland: Trans Tech Publ) pp 183–8
[93] Bonatti C and Mohr D 2019 *J Mech Phys Solids* **122** 1–26
[94] Verlee B, Dormal T and Lecomte-Beckers J 2013 *Powder Metall* **55** 260–7
[95] ASTM 2014 *Standard Specification for Additive Manufacturing Nickel Alloy (UNS N07718) with Powder Bed Fusion* URL www.astm.org
[96] Mukhtarov S and Ermachenko A 2010 Mechanical properties of nanostructured nickel based superalloy inconel 718 *J Phys Conf Ser* 240 (Bristol: IOP Publishing) p 012118
[97] Valdez M, Kozuch C, Faierson E and Jasiuk I 2017 *J. Alloys Compd.* **725** 757–64
[98] Tanaka H and Kunimura M 2002 *Polym. Eng. Sci.* **42** 1333–49
[99] Yuan S, Shen F, Bai J, Chua C, Wei J and Zhou K 2017 *Mater. Des.* **120** 317–27
[100] Phang I Y, Liu T, Mohamed A, Pramoda K P, Chen L, Shen L, Chow S Y, He C, Lu X and Hu X 2005 *Polym Int* **54** 456–64
[101] Lu X and Jin Y 2018 *Mater. Res. Express.* **5** 065301
[102] Neff C, Hopkinson N and Crane N 2018 *Addit Manuf* **22** 807–16
[103] Vacha J and Boruka M 2015 *NANOCON* **1** 132-137
[104] Khan M M K, Liang R, Gupta R and Agarwal S 2005 *Korea Aust. Rheol. J.* **17** 1–7
[105] Gautam R, Idapalapati S and Feih S 2018 *Mater. Des.* **137** 266–75
[106] Chen L and Zhang X 2019 *Appl. Surf. Sci.* **492** 765–75
[107] Iragi M, Pascual-González C, Esnaola A, Lopes C and Aretxabaleta L 2019 *Addit Manuf* **30** 100884
[108] Yánez A, Fiorucci M P, Cuadrado A, Martel O and Monopoli D 2020 *Int J Fatigue* **138** 105702
[109] Dinh T D, Vanwalleghem J, Xiang H, Erdelyi H, Craeghs T and Van Paepegem W 2020 *Addit Manuf* **33** 101139
[110] Sanaei N and Fatemi A 2020 *Mater. Sci. Eng.* A **785** 139385
[111] Aboulkhair N, Simonelli M, Parry L, Ashcroft I, Tuck C and Hague R 2019 *Prog. Mater. Sci.* **106** 100578
[112] Zhou L, Yuan T, Tang J, He J and Li R 2019 *Opt Laser Technol* **119** 105625
[113] Jap N, Pearce G, Hellier A, Russell N, Parr W and Walsh W 2019 *Int J Fatigue* **124** 328–37
[114] Bouzakis E, Arvanitidis A, Kazelis F, Maliaris G and Michailidis N 2020 *Procedia CIRP* **87** 469–73
[115] Biswal R, Syed A and Zhang X 2018 *Addit Manuf* **23** 433–42
[116] Smith T R, Sugar J D, Schoenung J M and San Marchi C 2019 *Mater. Sci. Eng.* A **765** 138268
[117] Le V D, Pessard E, Morel F and Prigent S 2020 *Int J Fatigue* **140** 105811
[118] Ferro P, Fabrizi A, Berto F, Savio G, Meneghello R and Rosso S 2020 *Theor. Appl. Fract. Mech.* **108** 102611
[119] Sheridan L, Scott-Emuakpor O, George T and Gockel J 2018 *Mater. Sci. Eng.* A **727** 170–6
[120] Wu M W, Chen J K, Lin B H, Chiang P H and Tsai M K 2020 *Mater. Sci. Eng.* A **790** 139695
[121] Kahlin M, Ansell H, Basu D, Kerwin A, Newton L, Smith B and Moverare J 2020 *Int J Fatigue* **134** 105497

[122] Babamiri B B, Indeck J, Demeneghi G, Cuadra J and Hazeli K 2020 *Addit Manuf* **34** 101380
[123] Poulin J R, Kreitcberg A, Terriault P and Brailovski V 2020 *Int J Fatigue* **132** 105394
[124] Blinn B, Krebs F, Ley M, Teutsch R and Beck T 2020 *Int J Fatigue* **131** 105301
[125] Pellizzari M, AlMangour B, Benedetti M, Furlani S, Grzesiak D and Deirmina F 2020 *Theor. Appl. Fract. Mech.* **108** 102634
[126] Romano S, Nezhadfar P, Shamsaei N, Seifi M and Beretta S 2020 *Theor. Appl. Fract. Mech.* **106** 102477
[127] Pegues J, Roach M, Williamson R S and Shamsaei N 2018 *Int J Fatigue* **116** 543–52
[128] González-Henríquez C, Sarabia-Vallejos M and Rodriguez-Hernandez J 2019 *Prog. Polym. Sci.* **94** 57–116
[129] Al-Ketan O, Rowshan R and Al-Rub R A 2018 *Addit Manuf* **19** 167–83
[130] Xu B, Yin S, Wang Y, Li H, Zhang B and Ritchie R 2017 *Compos. Part A Appl. Sci. Manuf.* **97** 41–50
[131] Singh A, Deptula A, Anawal R, Doddamani M and Gupta N 2019 *JOM* **71** 1520–7
[132] Li Y *et al* 2018 *Acta Biomater.* **77** 380–93
[133] Loh G, Pei E, Harrison D and Monzón M 2018 *Addit Manuf* **23** 34–44
[134] Gao W, Zhang Y, Ramanujan D, Ramani K, Chen Y, Williams C, Wang C, Shin Y, Zhang S and Zavattieri P 2015 *Comput. Aided Des.* **69** 65–89
[135] Terriault P and Brailovski V 2018 *Finite Elem Anal Des* **138** 1–11
[136] Takezawa A, Zhang X and Kitamura M 2019 *Int. J. Heat Mass Transf.* **143** 118564
[137] Yates J, Efthymiadis P, Antonysamy A, Pinna C and Tong J 2019 *Fatigue Fract Eng Mater Struct* **42** 2146–54
[138] Liu X and Shapiro V 2016 *Comput. Aided Des.* **78** 71–82
[139] D'Amico T, Barrett C, Presing J and Peterson A 2019 *Addit Manuf* **27** 91–8
[140] Xu Y, Ren S and Zhang W 2018 *Compos. Struct.* **193** 212–23
[141] O'Connor H and Dowling D 2018 *Addit Manuf* **21** 404–12
[142] Gockel J, Sheridan L, Koerper B and Whip B 2019 *Int J Fatigue* **124** 380–8
[143] Liu C, Zhang M and Chen C 2017 *Mater. Sci. Eng.* A **703** 359–71
[144] Türk D A, Brenni F, Zogg M and Meboldt M 2017 *Mater. Des.* **118** 256–65
[145] Chacón J, Caminero M, Núñez P, García-Plaza E, García-Moreno I and Reverte J 2019 *Compos Sci Technol* **181** 107688
[146] Schirmeister C, Hees T, Licht E and Mülhaupt R 2019 *Addit Manuf* **28** 152–9
[147] Heidari-Rarani M, Rafiee-Afarani M and Zahedi A 2019 *Compos. B. Eng.* **175** 107147
[148] Magri A E, Mabrouk K E, Vaudreuil S and Touhami M E 2019 *J. Thermoplast. Compos. Mater.* **1** 0892705719847244
[149] Lopes B and d'Almeida J 2019 *Mater. Today Proceed* **8** 719–30
[150] Akasheh F and Aglan H 2018 *J. Elastomers Plast.* **51** 698–711
[151] Agarwal K, Kuchipudi S, Girard B and Houser M 2018 *J Compos Mater* **52** 3173–81
[152] Papon E and Haque A 2019 *Addit Manuf* **26** 41–52
[153] Bland S and Aboulkhair N 2015 *Met. Powder Rep.* **70** 79–81
[154] Moussaoui K, Rubio W, Mousseigne M, Sultan T and Rezai F 2018 *Mater. Sci. Eng.* A **735** 182–90
[155] Yakout M, Cadamuro A, Elbestawi M and Veldhuis S 2017 *Int. J. Adv. Manuf. Technol.* **92** 2081–98
[156] Kumar P, Farah J, Akram J, Teng C, Ginn J and Misra M 2019 *Int. J. Adv. Manuf. Technol.* **103** 1497–507
[157] Garg A, Lam J and Savalani M 2015 *Int. J. Adv. Manuf. Technol.* **80** 555–65
[158] Furumoto T, Koizumi A, Alkahari M, Anayama R, Hosokawa A, Tanaka R and Ueda T 2015 *J Mater Process Technol* **219** 10–6
[159] Fayazfar H, Salarian M, Rogalsky A, Sarker D, Russo P, Paserin V and Toyserkani E 2018 *Mater. Des.* **144** 98–128
[160] Cunningham R, Narra S, Montgomery C, Beuth J and Rollett A 2017 *JOM* **69** 479–84
[161] du Plessis A 2019 *Addit Manuf* **30** 100871
[162] Iebba M, Astarita A, Mistretta D, Colonna I, Liberini M, Scherillo F, Pirozzi C, Borrelli R, Franchitti S and Squillace A 2017 *J. of Materi Eng and Perform* **26** 4138–47
[163] Allison J, Sharpe C and Seepersad C 2019 *Addit Manuf* **25** 239–51
[164] Uddin S, Murr L, Terrazas C, Morton P, Roberson D and Wicker R 2018 *Addit Manuf* **22** 405–15
[165] Eiliat H and Urbanic J 2018 *Int. J. Adv. Manuf. Technol.* **96** 4095–109
[166] Parenti P, Cataldo S, Grigis A, Covelli M and Annoni M 2019 *Procedia Manuf.* **34** 738–46
[167] Fidan I, Imeri A, Gupta A, Hasanov S, Nasirov A, Elliott A, Alifui-Segbaya F and Nanami N 2019 *Int. J. Adv. Manuf. Technol.* **102** 1801–18
[168] Plott J, Tian X and Shih A 2018 *Addit Manuf* **22** 606–17
[169] Ahmed S, Hussain G, Al-Ghamdi K and Altaf K 2019 *J. Thermoplast. Compos. Mater.* **1** 0892705719869407
[170] Gisario A, Kazarian M, Martina F and Mehrpouya M 2019 *J Manuf Syst* **53** 124–49
[171] Galarraga H, Lados D, Dehoff R, Kirka M and Nandwana P 2016 *Addit Manuf* **10** 47–57
[172] Ziaee M and Crane N 2019 *Addit Manuf* **28** 781–801
[173] Hazeli K, Babamiri B, Indeck J, Minor A and Askari H 2019 *Mater. Des.* **176** 107826
[174] Ma C *et al* 2017 *J Mater Process Technol* **249** 433–40
[175] Deng D, Moverare J, Peng R and Söderberg H 2017 *Mater. Sci. Eng.* A **693** 151–63
[176] Ran X, Liu D, Li J, Liu X, Wang H, Cheng X, He B and Tang H 2018 *Mater. Sci. Eng.* A **723** 8–21
[177] Li Y, Cheng X, Liu D and Wang H 2018 *Mater. Sci. Eng.* A **713** 75–80
[178] Girelli L, Tocci M, Gelfi M and Pola A 2019 *Mater. Sci. Eng.* A **739** 317–28
[179] Plott J and Shih A 2017 *Addit Manuf* **17** 1–14
[180] Gangireddy S, Faierson E and Mishra R 2018 *J. Dyn. Behav. Mater.* **4** 441–51
[181] Shamsaei N, Yadollahi A, Bian L and Thompson S 2015 *Addit Manuf* **8** 12–35
[182] Kang Y J, Yang S, Kim Y K, AlMangour B and Lee K A 2019 *Corros Sci* **158** 108082
[183] Larrosa N, Wang W, Read N, Loretto M, Evans C, Carr J, Tradowsky U, Attallah M and Withers P 2018 *Theor. Appl. Fract. Mech.* **98** 123–33
[184] Joseph J, Hodgson P, Jarvis T, Wu X, Stanford N and Fabijanic D 2018 *Mater. Sci. Eng.* A **733** 59–70
[185] Seifi M, Salem A, Satko D, Ackelid U, Semiatin S and Lewandowski J 2017 *J. Alloys Compd.* **729** 1118–35
[186] Niku-Lari A 1987 Overview on the shot peening process *Advances in Surface Treatments* (Amsterdam: Elsevier) pp 155–70
[187] Luo W, Noble B and Waterhouse R 1987 The effect of shot-peening intensity on the fatigue and fretting-fatigue behaviour of an aluminium alloy *Advances in Surface Treatments* (Amsterdam: Elsevier) pp 145–53
[188] Leuders S, Meiners S, Wu L, Taube A, Tröster T and Niendorf T 2017 *J Mater Process Technol* **248** 130–42
[189] Sadeghi E, Karimi P, Momeni S, Seifi M, Eklund A and Andersson J 2019 *Mater Charact* **150** 236–51

[190] Åsberg M, Fredriksson G, Hatami S, Fredriksson W and Krakhmalev P 2019 *Mater. Sci. Eng.* A **742** 584–9
[191] ASTM 2018 *Standard for Additive Manufacturing—Post Processing Methods—Standard Specification for Thermal Post-Processing Metal Parts Made Via Powder Bed Fusion* URL www.astm.org
[192] Kan W, Nadot Y, Foley M, Ridosz L, Proust G and Cairney J 2019 *Addit Manuf* **29** 100805
[193] Levenhagen N and Dadmun M 2018 *Polymer* **152** 35–41
[194] Spreeman M, Stretz H and Dadmun M 2019 *Addit Manuf* **27** 267–77
[195] Balla V, Kate K, Satyavolu J, Singh P and Tadimeti J 2019 *Compos. B. Eng.* **174** 106956
[196] Al-Maharma A and Sendur P 2018 *Mater. Res. Express* **6** 022001
[197] Al-Maharma A and Al-Huniti N 2019 *J. Compos. Sci.* **3** 27
[198] Golbang A, Harkin-Jones E, Wegrzyn M, Campbell G, Archer E and McIlhagger A 2020 *Addit Manuf* **31** 100920
[199] Street D, Mah A, Patterson S, Pickel D, Bergman J, Stein G, Messman J II and Kilbey S M II 2018 *Polymer* **157** 87–94
[200] Ning F, Cong W, Hu Z and Huang K 2017 *J Compos Mater* **51** 3733–42